Spatial Reconstruction of Electrons with an Accordion Geometry Electromagnetic Calorimeter

by

John S. White
B.Sc., University of Victoria, 1991.

A thesis submitted in partial fulfillment
of the requirements for the degree of
Master of Science
in the Department of Physics and Astronomy.

We accept this thesis as conforming
to the required standard.

Dr. M. Lefebvre, Supervisor (Department of Physics and Astronomy)

Dr. L. Robertson, Departmental Member (Department of Physics and Astronomy)

Dr. C. Qian, Outside Member (Department of Chemistry)

Dr. D. Axen, External Examiner (Department of Physics, University of British Columbia)

Supervisor: Dr. M. Lefebvre

Abstract

The spatial reconstruction performance of an accordion geometry calorimeter prototype was studied. The effectiveness of the upcoming ATLAS detector in observing new physics signals at LHC will depend on this attribute of the calorimeter. The performance parameters that describe the ability of the accordion calorimeter prototype to reconstruct the position and angle of electrons were calculated. Geometrical effects due to the accordion geometry were observed in both Monte Carlo and experimental data. The position reconstruction performance found after correcting for these effects is $\sigma_x = (137 \pm 81) \oplus (2981 \pm 327)/\sqrt{E}$ μm and the angular reconstruction performance is $\sigma_\theta = (67.4 \pm 2.5)/\sqrt{E} \oplus (139 \pm 57)/E$ mrad.

Examiners:

Dr. M. Lefebvre, Supervisor (Department of Physics and Astronomy)

Dr. L. Robertson, Departmental Member (Department of Physics and Astronomy)

Dr. C. Qian, Outside Member (Department of Chemistry)

Dr. D. Axen, External Examiner (Department of Physics, University of British Columbia)

Table of Contents

List of Tables

List of Figures

Preface

This thesis work is based on my involvement with the RD3 group at CERN in the latter half of 1992. During that period I took part in tests of a cartesian accordion prototype that produced the data used in this thesis. My supervisor and I installed and thoroughly tested the electronics on the prototype before it was placed in the cryostat. During the test period I was assigned shifts and learned how to run the data aquisition system. I was present when the readout chain was timed with respect to the beam and trigger and assisted in this task. In the course of my analysis of the cartesian prototype data I encountered and fixed some faults in the general RD3 analysis code. These modifications were incorporated into the base CERN version of the code.

I returned to CERN later in the year to take shifts in the pointing accordion prototype test period. With the experience gained in the previous test period I was able to take on more responsibilities such as the initial testing and calibration of the beam chambers. I also assisted in debugging the new trigger system and solved specific problems found in the online data analysis. One of the software duties I had was to finalise a program that read the accordion database in order to monitor calibration constants. I also wrote code that predicts the particle impact on the pointing prototype using precise survey information along with beam chamber and positioning measurements of the calorimeter. This task was successfully completed and will hopefully be used in future analyses.

During these two test periods I worked with many RD3 collaborators. I was then exposed to forefront calorimetry technology. Also during my stay at CERN I met many other people involved in the LHC effort and learned of the many other challenges facing this project.

I would like to thank my supervisor, Dr. Michel Lefebvre, for his advice, help with my work, patient proofreading, and making my integration into CERN so easy. In addition I would also like to acknowledge his development of the comprehensive and easy to use Monte Carlo simulations of the calorimeter prototype. My work in RD3 was made enjoyable and interesting by all the knowledgeable people in this group. Many thanks go to my fellow office inmates for their insights and proofreading.

I must also not forget Penny, Ginger, Meg and Tinker for waiting up until I got home.

Chapter 1

Introduction

The high energy physics community is currently planning new particle colliders that will allow physicists to probe the laws of nature down to the TeV mass scale [1]. The Large Hadron Collider (LHC) planned at CERN [2] in Geneva, Switzerland, will provide proton-proton collisions of 14 TeV center of mass energy. Detectors such as the one proposed by the ATLAS collaboration are needed to exploit these collisions. The planned ATLAS detector is part of a general purpose experiment designed to take full advantage of the discovery potential of the LHC.

The RD3 group, working within the ATLAS collaboration, has put forward a proposal for an electromagnetic calorimeter, a detector subsystem that measures electromagnetic energy. This calorimeter relies on a novel accordion geometry and optimised electronic readouts to meet the criteria set by the LHC experimental environment. The RD3 group has carried out several tests on accordion calorimeter prototypes in the past to evaluate their performance.

The work presented in this thesis stems from a test of a prototype at CERN

---

[1] Natural units with $\hbar = c = 1$ are used throughout unless otherwise stated.

[2] Centre Européen pour la Recherche Nucléaire.

that took place in the summer of 1992. In particular the spatial reconstruction performance of this prototype for electrons is studied. The ability of the ATLAS detector to observe signatures of new physics at LHC depends on this feature of the calorimeter.

Chapter 2 reviews the Standard Model of particle physics and the motivations for building LHC and the ATLAS detector. LHC and ATLAS are then reviewed, and the expected physics signals at LHC are briefly described. The requirements of calorimetry at LHC and the basic principles of calorimetry are also outlined. Chapter 3 contains the description of the accordion concept and of the prototype used, along with a description of the accordion electromagnetic calorimeter for ATLAS. Chapter 4 treats the spatial reconstruction performance of the prototype obtained from experimental data. Descriptions of the test beam set up and analysis tools and methods are included. Conclusions, pertaining to ATLAS and future tests, are presented in chapter 5.

Chapter 2

Physics with ATLAS at LHC

2.1 The Standard Model

In the manner that the electric and magnetic forces were united by Maxwell in the 1860's, the weak and electromagnetic forces were united by Glashow, Weinberg and Salam in 1961 [1]. The standard model of electroweak interactions between elementary particles is based on a spontaneously broken $SU(2) \times U(1)$ gauge theory [1]. The addition of the $SU(3)$ group that describes strong interactions gives the Standard Model (SM). There are two types of particle in the SM: the fermions that constitute all matter, and the bosons that mediate forces. The forces that govern the behaviour of the fermions are the electromagnetic, the weak and the strong forces. These forces are transmitted by mediators of varying masses: the electromagnetic force by the massless *photon*; the weak force, responsible for β-decays, by massive $W^{\pm}$ and Z particles [2, 3]; and the strong force, that binds nuclei, by colour charge carrying massless *gluons*.

In the SM the masses of the mediators and fermions are generated after the spontaneous symmetry breaking of the vacuum via the *Higgs mechanism* [4], producing a massive neutral scalar Higgs boson. The Higgs boson (H^0) has not yet

Table 2.1: Leptons and quarks arranged in generations of increasing mass. Lepton and quark masses from [5]. The top quark has not been directly observed.

Leptons			Quarks		
Name	Mass (MeV)	Charge (e)	Name	Mass (MeV)	Charge (e)
electron (e)	0.511	-1	up	5.6 ± 1.1	$+2/3$
ν_e	< 0.000017	0	down	9.9 ± 1.1	$-1/3$
muon (μ)	106	-1	charm	1350 ± 50	$+2/3$
ν_μ	< 0.27	0	strange	199 ± 33	$-1/3$
tau (τ)	1784	-1	top	?	$+2/3$
ν_τ	< 35	0	bottom	~ 5 GeV	$-1/3$

been observed experimentally [6], but LEP data [7] has put a lower bound on the Higgs mass of 62.5 GeV.

The fermions that make up all matter are divided into two groups, the leptons and quarks. Leptons and quarks are subdivided again into three generations shown in table 2.1. Leptons carry integer electric charge and feel the electroweak force. Quarks carry colour charge and non-integer electric charge feel in the electroweak and strong forces. Due to the structure of the strong force a single free quark can never be observed. Quarks appear in the SM in combinations that give no net colour charge. The fermions have corresponding antifermions. The top quark, essential for the consistency of the SM, has not yet been observed experimentally but current data [8, 9] limits its mass m_t to $108 < m_t < 200$ GeV. Transitions between quark generations are observed. They are described in the SM with the 3×3 Cabibbo-Kobayashi-Maskawa (CKM) matrix [10].

Following the discovery of the $W^{\pm}$ and Z vector bosons at the CERN $p\overline{p}$ collider [2, 3], the SM has been tested to unprecedented precision by the experimental results obtained from the four experiments at LEP [11]. The SM proves to be a model capable of precise predictions at the microscopic level. However it is universally accepted that the SM cannot be the last word, although no viable extension of the SM has emerged. Furthermore the top quark and the Higgs boson have not been observed yet. Some of the proposed extensions of the SM, for example Supersymmetry (SUSY), bring a rich spectrum of particles which await discovery. In this situation high energy hadron colliders, such as LHC, which have centre of mass energies in the multi-TeV range, have the best potential for future discovery.

2.2 LHC

The Large Hadron Collider (LHC) is the next major project planned by CERN [12]. This collider is to be located in the existing LEP tunnel. The colliding particles are protons with a center-of-mass energy of 14 TeV. A second mode of operation for the LHC as a heavy ion collider will be possible. This collider makes extensive use of the existing facilities at CERN. The constraint of the diameter of the LEP ring places a demand on the guide field of the bending magnets required for LHC operation at 14 TeV, which must be in the region of 8.5 T.

The use of protons as projectiles has the following advantages:

- Synchrotron radiation losses for protons are much less than for electrons of the same energy [12];
- Protons are easier to produce than antiprotons and at high energies the cross section σ_t is equal for pp and $p\overline{p}$ collisions;
- A hadron collider offers excellent discovery potential due to the nature of the collisions. At high energies the proton momentum is split equally between gluons and quarks that allow a diverse spectrum of collisions.

LHC is designed to run at the high particle rate or *luminosity* (defined as the number of particles per cm^2 per second, $\mathrm{cm}^{-2}\mathrm{s}^{-1}$) of 10^{34} $\mathrm{cm}^{-2}\mathrm{s}^{-1}$ because the cross sections for the most sought after physics signals are very small.

Characteristically the experiments at LHC consist of large detectors with precise inner tracking, followed by electromagnetic then hadronic calorimetry, and finally muon detectors. The calorimetry must be as hermetic as possible in order to make the detection of missing transverse energy (E_T^{miss}) efficient. These detectors must be physically large to contain the high energy interaction products. They must have a fast response time to cope with the high luminosity and low bunch crossing times of the colliders. The prototype tested in this work is part of the electromagnetic calorimeter proposal for the ATLAS detector at LHC.

2.2.1 ATLAS

The ATLAS detector [13, 14] (see figure 2.1) is designed as a general purpose detector with a balanced approach to detection of electrons, muons, jets and missing transverse energy. The detector is optimized to provide as many signatures as possible for new physics at the highest LHC luminosity, while at the same time retaining good performance at the lower initial luminosities. The magnet choice consists of an outer muon toroid, complemented by an inner solenoid. This choice of magnets places almost no constraints on the calorimetry and inner detector allowing flexibility for technological choices.

At LHC lepton identification is crucial. Even if the final state lepton rate is often expected to be small for many processes, leptons will give the cleanest signals. At a luminosity of 10^{34} $\mathrm{cm}^{-2}\mathrm{s}^{-1}$ there will be very large background rates which will mask these lepton signatures. Muons are easy to identify since they go through the

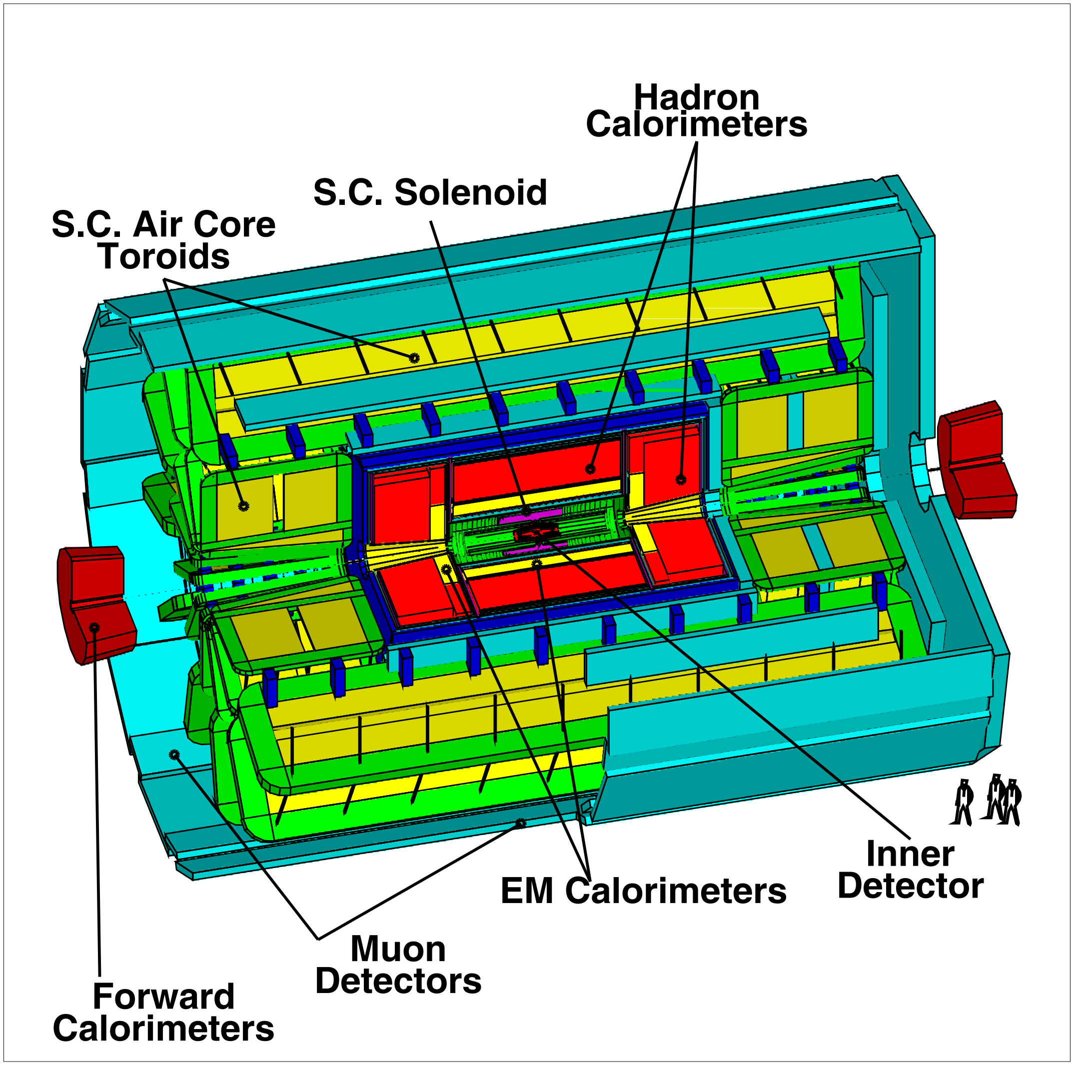

Figure 2.1: The proposed ATLAS detector.

detector without showering. They can also be separated from jets, but their momentum is hard to obtain precisely. Electrons energy and momentum are relatively easy to measure but electrons are hard to identify at high luminosity due to the ability of jets (pions) to fake electron signatures. The ATLAS detector at LHC makes use of good calorimetry for electron and photon identification and E_T^{miss} measurements, which will rely on good measurements of EM shower energy and position over a wide acceptance range.

The particle multiplicity at hadron colliders is approximately constant over *pseudorapidity*, defined as

$$\eta = -\ln\left(\tan\frac{\theta}{2}\right) ,$$

where θ is the polar angle. Thus η is the natural variable to use when describing the polar coordinate. The azimuthal angle ϕ is used as in spherical coordinates.

2.2.2 Physics signatures at LHC

One of the benchmark processes affecting the design of LHC and ATLAS is the detection of the SM Higgs boson [6, 14]. The mass of the Higgs boson plays a major role in determining the decay modes which may be used for its detection. For a low to intermediate Higgs boson mass (50 to 200 GeV) the decay $H^0 \rightarrow \gamma\gamma$ is the most promising. Up to about 90 GeV the decay modes $H^0 \rightarrow W^*W$ and Z^*Z become important. A heavy Higgs boson of 200 to 1000 GeV has $H^0 \rightarrow W^+W^-$ and $H^0 \rightarrow ZZ$ as the dominant decay modes. The detection of a heavy H^0 depends on the ability to detect e, μ and ν_e, ν_μ (via missing transverse momentum P_T^{miss}) and jets. The H^0 production in this regime is resonant and the H^0 width in the low and intermediate mass range is narrow, but it becomes broad at high mass [15]. This is an important consideration for the design of experiments at the LHC.

The other missing particle of the SM, namely the top quark, can be studied at

LHC. SM analyses, along with LEP precision data and M_W/M_Z from $p\overline{p}$ colliders, predict that the top quark mass (m_t) is in the range 100-200 GeV [8, 9]. Thus the top quark could be discovered at the LHC if it has not been found at the Fermilab Tevatron. At the LHC energy the cross section for top production is $\sigma_{t\overline{t}} = 3$ nb for m_t of 140 GeV, thus large numbers of $t\overline{t}$ pairs will be produced even at a luminosity of $10^{32}\mathrm{cm}^{-2}\mathrm{s}^{-1}$. Even if the top quark has already been discovered, its mass will not be measured to a precision of better than 10 GeV. The electroweak measurements at LEP, combined with an accurate measurement of $\mathrm{m_t}$, can be used to set limits on the mass of H^0.

Possible signatures of the top quark include $t\overline{t} \rightarrow WW + b$-jets with one W decaying to $\ell\,\nu$ and the other to $q\overline{q}'$. Another possible signal is $t\overline{t} \rightarrow WW + b$-jets, with one W decaying to $\mu\nu$ and the other to $e\nu$. In both these channels good lepton tracking and momentum resolution are essential.

If a charged Higgs boson exists it may be produced through the decay mode $t \rightarrow b\,H^+$ [16] where the H^+ decays to either $c\overline{s}$ or $\tau\,\nu_\tau$. The $\tau\,\nu_\tau$ channel can be studied by searching for a clean sample of $t\overline{t}$ events with a high transverse energy lepton (e or μ).

Squarks and gluinos, the strongly interacting supersymmetric (SUSY) particles, have large production cross sections at LHC [17]. The common characteristic of SUSY decays is the combination of jets and E_T^{miss}. This signature remains the most promising for the detection of gluinos and squarks.

Searches for heavy Z' and W' can be made at LHC. A mass range of several TeV can be explored [13]. These particles appear in a number of models, e.g. minimal extensions of the SM and models for electroweak symmetry breaking through compositeness. The Z' can decay through $Z' \rightarrow e^+\,e^-$ or $\mu^+\mu^-$ allowing a straightforward reconstruction of the Z' mass.

The mass reconstruction by ATLAS of as yet undiscovered particles is carried out by the observation of the energies and directions of their decay products. The energy measurement is crucial in this respect. Furthermore, the detection of missing transverse energy infers the presence of neutrinos (ν's), present in some of the above decays. Energy measurements are carried out with a *calorimeter*.

2.3 Calorimetry at LHC

A calorimeter is a device that absorbs energy and produces a signal proportional to this energy. This signal can be either an electrical, optical, thermal or acoustical and with an appropriate calibration the absorbed energy is determined. In high energy physics particles lose energy in matter by various methods, mediated by the electromagnetic, strong or weak forces.

The loss of energy governed by the electromagnetic (EM) force is considered first. The energy loss of a electron (or positron) incident on a block of matter depends on its initial energy. At high energies the dominant energy loss mechanism is brehmsstrahlung: the emission of an energetic photon (E_γ) through the scattering of an electron on the coulomb field of a nucleus of charge Ze. The number of photons between the energy E_γ and $(E_\gamma + dE_\gamma)$ is given by [18]

$$N(E_\gamma)dE_\gamma \propto Z^2 \frac{dE_\gamma}{E_\gamma} \tag{2.1}$$

and is therefore dependent on the material in which the electron interacts. The *radiation length* (X_0) is the distance that an electron travels in a material such that its energy is reduced by a factor e by brehmsstrahlung. This important quantity is dependent on the material in which the energy is lost and can be approximated [19] by

$$X_0 = \frac{716.4\mathrm{g\,cm}^{-2} A}{Z(Z+1)\ln 287/\sqrt{Z}},$$

where A is he mass number of the nucleus. Energy loss by brehmsstrahlung dominates for electrons above a critical energy ϵ_c approximated by [20]

$$\epsilon_c = \frac{800\mathrm{MeV}}{Z+1.2}.$$

For an energy below ϵ_c electrons will lose energy primarily through ionization. The rate of energy loss by this mechanism, for a particle of mass M and charge ze, is given by the Bethe-Bloch equation [21]

$$\frac{dE}{dx} = \frac{4\pi N_0 z^2 e^4}{m\beta^2}\frac{Z}{A}\left[\ln\left(\frac{2m\beta^2}{I(1-\beta^2)}\right) - \beta^2\right], \tag{2.2}$$

where m is the electron mass, β is the velocity of the particle, N_0 is Avogadro's number, Z and A are the atomic number and atomic weight of the atoms in the medium, x is the path length multiplied by the density of the medium and E is the energy loss. I is a global ionization potential approximately given by $10Z$ eV. dE/dx as described by equation 2.2 passes through a minimum at $E \simeq 3M$. A particle with this energy is called a *minimum ionizing* particle.

The energy loss of photons is subject to different mechanisms. The three principal energy loss processes for photons have differing dependences on the photon energy E_γ. The photoelectric effect has a dependence of $1/E_\gamma^3$, Compton scattering (scattering of a photon off an atomic electron) goes as $1/E_\gamma$, and electron-positron pair production is essentially energy independent above 1 MeV. Thus at high energies of $E_\gamma > 10$ MeV photons will lose predominantly through electron-positron pair production. In the same manner as X_0 for the electrons, a characteristic length for photons, the *conversion length* l_γ, is defined as the distance over which the intensity of a photon beam is reduced by a factor of e. It is given by [21]

$$l_\gamma \simeq 9X_0/7\,.$$

Photons above the critical energy ϵ_c predominantly convert into two charged particles while those below interact through Compton scattering only.

At $E_\gamma < 10$ MeV the Compton scattering (the scattering of a photon from an atomic electron) and photoelectric effect (photon absorption and subsequent electron ejection by an atom) become important. Compton scattered and photoelectric ejected electrons will in turn lose energy through ionization until these losses reduce their energy below the ionization potential of the medium where they are ionically absorbed. Very low energy photons will lose energy through Rayleigh scattering (scattering of a photon from a whole atom) and eventually exit the material.

An *electromagnetic shower* develops in matter via the processes described above. A high energy ($E_e \gg \epsilon_c$) electron incident on matter will lose energy through brehmsstrahlung until its energy E_e reaches ϵ_c. The brehmsstrahlung photons, themselves of energy $E_\gamma \gg 10$ MeV, are most likely to convert to electron-positron pairs that will in turn brehmsstrahlung again. At this stage the electromagnetic shower is developing; the number of particles is increasing and the lateral dimensions are increasing by virtue of the scattering processes. Once the energy of the electrons, positrons and photons fall to ϵ_c the particle multiplication ceases. At this stage electrons and positrons lose energy through ionization, photons interact through Compton and Rayleigh scattering and photoelectric effect. Thus a single electron incident on a block of matter will produce a shower of secondary particles. For an incident photon the showering process is identical, except that the photon initially converts to a electron-positron pair.

The behaviour of EM showers has been studied by Rossi [22]. From this treatment of EM showers (Rossi's approximation B) the following conclusions are obtained:

- The total length of all ionizing tracks in a shower is directly proportional to the incident particle energy E;
- The centre of gravity in depth of a shower depends on $\ln E$;
- The depth of the peak of the shower scales with $\ln E$;
- The number of particles at the peak of the shower scales with $1/\ln(E^{\frac{1}{2}})$.

In a sampling calorimeter the statistical fluctuations of an EM shower are reduced as more energy is sampled. Hence the accuracy of measuring the energy of an EM shower depends on a good sampling and a good shower containment in the calorimeter.

The lateral scale of an EM shower is characterised by the *Molière radius* R_M given by [5]

$$R_M = 21.2\,\mathrm{MeV}(X_0/\epsilon_c)\,,$$

where ϵ_c is in MeV. An EM shower is assumed to be contained in a cylinder of radius $2R_M$ for the purpose of total energy measurement. The measurement of shower position is intrinsically accurate due to its dependence on the angle ψ of electron-positron pairs created by a photon of energy E_γ that scales with

$$\psi \propto m_e \frac{\ln E_\gamma/m_e}{E_\gamma}\,,$$

where m_e is the electron mass. The statistical shower fluctuations can be minimised in position measurements by considering as many shower particles as possible and the final accuracy is dependent on the size of the calorimeter cells [23].

For the interaction of hadrons in matter the process is far more complicated due to the nature of the processes at work. An incident hadron encounters a nucleon that recoils, initiating a hadronic cascade [24] that has an widely varying electromagnetic component (π^0's and η's) (generally 1/3 of the produced particles [25]). The π^0's and η's will decay predominantly to 2γ [5] and initiate electromagnetic showers. The hadronic component will continue through the matter, losing energy through ionization and other nuclear collisions that may produce more EM showers. Hadronic interactions in matter depend on the nuclear density of the medium and the characteristic length λ_{int} scales with $A^{1/3}$. Characteristically λ_{int} is larger than X_0 and this difference in scale allows distinction between EM and hadronic showers.

A hadronic shower is characterised by electromagnetic components produced by hadronic interactions, distributed in depth according to λ_{int}. The lateral dimensions of hadronic showers are much broader than the EM case due to the nature of nuclear collisions that produce particles at large angles to the particle direction of incidence.

For example a process such as $H^0 \rightarrow \gamma\gamma$ could be observed in the ATLAS detector at LHC. The H^0 mass could then be determined by the observation of the two photon showers. The detection of electromagnetic and hadronic showers with a calorimetry system is crucial for many sought for processes [14]. The LHC environment sets stringent requirements for effective calorimetry

2.3.1 Calorimetry requirements in ATLAS

At LHC one of the major considerations for calorimetry and overall detector performance is the effect of pile-up due to the high luminosity and low bunch crossing time. For a luminosity of 10^{34} cm^{-2}s^{-1} and bunch crossing time of 25 ns, on average 15 events are expected per bunch crossing, each with more than 30 charged particles produced. Slow detectors may integrate over several bunch crossings. To limit the effect of pile-up (for slow readout) and electronics noise (for fast readout) on the detector an optimum readout time must be used, typically around $\sim$ 40 ns.

The general calorimeter design needs to be optimized according to the luminosity of the collider. Since the speed of the calorimeter has a lower limit of 2 bunch crossings, the effect of ~ 30 events in the calorimeter has to be studied. The size of a calorimeter cell determines the probability that the cell contains less than a certain pile-up energy which will act as noise over which signal (jets, isolated electrons, etc.) will have to be measured. To limit the effects of pile-up on the calorimetry the granularity of the EM calorimeter should be $\Delta\eta \times \Delta\phi = 0.025 \times 0.025$ which allows 95% of the shower energy to be contained in a 3×3 cell cluster [13].

The LHC environment demands high performance from the calorimeter. This is especially true for low and intermediate mass Higgs searches using the decay modes $H^0 \to \gamma\gamma$ and $H^0 \to Z^*Z$, where each Z decays to $\mathrm{e}^+\mathrm{e}^-$. Clearly adequate resolution is needed for the observation of m_H and Γ_H. High performance does not only imply high resolution; it is also important to have a very large rejection ($\sim 10^4$, in conjunction with inner tracking) against jet background which can fake photons. A calorimeter capable of making isolation cuts can identify γ's as opposed to jet fragments resulting in a high position resolution which helps distinguishing single γ's from $\pi^0 \to \gamma\gamma$.

The directional resolution is also an important consideration in the performance of the calorimeter. In the cases of $H^0 \to \gamma\gamma$, especially if the event vertex is not known, the H^0 mass resolution depends strongly on the knowledge of the direction of the photons. In order to achieve an adequate energy resolution, a directional resolution of at least $\sigma_\theta \sim 100\,\mathrm{mrad}/\sqrt{E}$ is required [26].

Due to the radiation that will be present in the LHC experimental areas [13] the calorimetry technique will have to be radiation hard. Furthermore, the large number of channels in the calorimetry require its calibration to be easy and stable.

With the emphasis on electron and photon identification and momentum measurements the EM calorimetry for the ATLAS detector plays a crucial role in the overall detector performance. Several requirements are placed on the EM calorimetry [13].

- To make measurements of missing transverse energy E_T^{miss} as accurate as possible the hermeticity of calorimetry coverage must be maximised.

- The energy resolution must be good. The energy resolution performance σ_E may be parameterised as

  $$\frac{\sigma_E}{E} = a \oplus \frac{b}{\sqrt{E}} \oplus \frac{c}{E}$$

  where a, b and c are the constant, sampling and noise terms respectively. At high energies a (related to the cell to cell calibration, uniformity of response and stability with time) dominates and a term of $\sim$ 1% is aimed for. A sampling term with $b = 10\,\%\,\mathrm{GeV}^{\frac{1}{2}}$ is required. At low energy, the noise term limits the energy resolution.

- To enable the ATLAS detector to trigger on interesting lepton events the granularity of the EM calorimeter must be adequate for electron identification and separation of electrons from backgrounds. The granularity required is $\Delta\eta \times \Delta\phi = 0.025 \times 0.025$.

- The energy response of the calorimeter should be uniform over all areas to limit the effect on the energy resolution (above) and also allow fast triggering on events with no secondary processing of data.

- Stability of the calorimeter over time is important to limit the frequency of calibration.

The EM calorimetry technique selected by ATLAS is based on liquid argon sampling calorimetry.

2.4 Principles of Liquid Argon Calorimetry

There are two basic types of calorimeters used in high energy physics. The *total absorption* calorimeter is made of a homogeneous material acting as *absorber* and *active material* at the same time (eg. lead glass calorimeters). The other calorimeter type is the *sampling* calorimeter. In this technique the energy of the incident particle is also completely absorbed in the calorimeter but only a fraction is sampled in an active material; the absorbers are made of materials that promote the release of energy into the active sampling layers.

The advantage of sampling calorimeters is that they can be made very compact using dense absorber planes which is very useful when the calorimeter is used as a detector subsystem. Another advantage of sampling calorimeters is the possibility of a fine segmentation which is crucial for particle identification and spatial reconstruction.

A calorimeter that determines energy by detecting the ion pairs produced by ionizing particles needs to have an active material that collects a reasonable fraction of the deposited charge to improve the signal to noise ratio [27]. Therefore the material must be dense, not attach electrons and have a relatively high electron mobility. The absorber material must be one that enhances the shower process: ie. a short radiation length X_0 in the case of EM calorimetry or short interaction length λ_{int} for hadronic calorimetry.

Liquid argon (LAr) is selected as the sampling material for the ATLAS EM calorimeter for the following reasons:

- It is dense (1.4 g/cm^3);
- It has a relatively high electron mobility ($\sim$ 5 mm/μs at 1kV/mm) and does not attach electrons;

- The ionization potential of 23.6 eV [28] allows the production of great numbers of ion pairs;
- It is easy to obtain and purify, resulting in relatively low cost (compared to liquid krypton or liquid xenon);
- It is inert and many electronegative impurities are frozen out at liquid temperature;
- It is radiation hard which is important for the LHC environment.

Lead is selected as the absorber for the following reasons:

- It has a short (0.56 cm) radiation length allowing the calorimeter to be compact;
- It is easy to machine, cheap and radiation hard;
- It is relatively non-toxic (compared to uranium, another common absorber).

Thus a calorimeter of lead absorbers interlaced by sampling LAr can be constructed to measure the energy and position of EM showers in ATLAS.

2.4.1 A simple liquid argon cell

The basic principles of LAr calorimetry can be illustrated with a simple cell similar to those in the calorimeter used in this study (see figure 2.2). The lead absorbers at each edge of the cell are held at ground potential and function as short X_0 EM shower inducers. A readout electrode consisting of outer layers at high voltage and a capacitively coupled inner layer is placed at distance d between the absorbers.

A minimum ionizing particle that traversing the cell will deposit energy in both the liquid argon gap and the absorber plates along its path through the cell. The

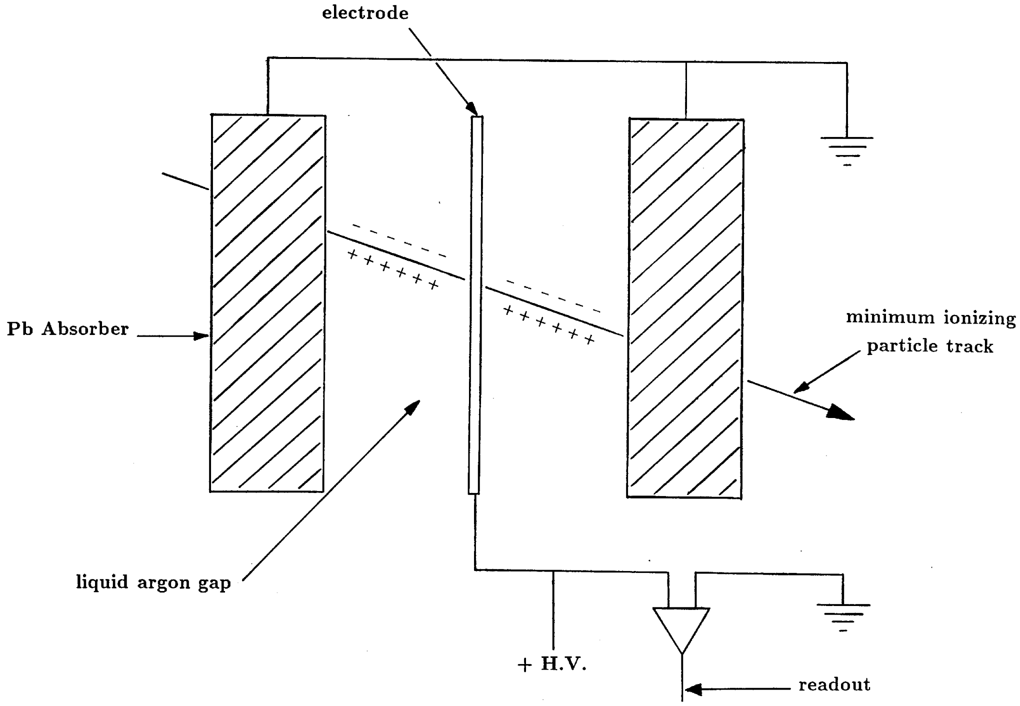

Figure 2.2: A simple lead-liquid argon cell.

rate of energy loss is given by equation 2.2 and an ion pair (e^-, Ar^+) will be created in the liquid argon for every 23.4 eV deposited. With an energy loss of 2.11 MeV/cm a large number N of such pairs are created evenly between the absorbers and the readout electrode. The electrons produced in the gap will drift and induce a current i_d at the readout electrode initially proportional to the number of ions produced in the gap. The electrons drift towards the positive potential on the electrode with a drift velocity v_d. The current i_d will decrease linearly as electrons reach the electrode. The total charge collected on the readout electrode is found to be $Ne/2$ [27], proportional to the energy deposited in the cell by the ionizing particle.

The energy deposited in the absorbers is lost but knowing the fraction of energy lost in the sampling material (LAr) to that in the absorber (lead), the *sampling fraction*, this lost energy can be calibrated out on average.

A EM shower is made up of many such ionizing tracks (see section 2.3) and by having many of these cells placed along the shower direction, a *parallel plate* calorimeter, all the ionizing track energy can be read in this manner. In this case, if the shower is completely contained in the calorimeter, the current i_d is proportional to the energy of the incident particle producing the EM shower [22].

The geometry of the LAr-Pb sampling calorimeter planned for ATLAS follows an 'accordion' geometry and is described next.

Chapter 3

The Accordion Geometry Calorimeter

The issues of granularity, ease of calibration, radiation hardness and stability can be readily addressed by liquid argon (LAr) sampling calorimetry [27]. The use of LAr as active material solves the problem of detector stability and radiation hardness. The response of LAr to ionizing particles is uniform provided contamination is controlled which allows straightforward calibration of the calorimeter. Fast readout and good hermeticity are made possible by a new accordion geometry concept.

The accordion electromagnetic (EM) calorimeter is a Pb-LAr sampling calorimeter. Lead, with its short (0.56 cm) radiation length, is used as absorber for the production of electromagnetic showers while LAr is the sampling medium. The absorbers and readout planes are not perpendicular to the incident particle but are folded in an accordion shape and run parallel to the particle direction (see figure 3.1.)

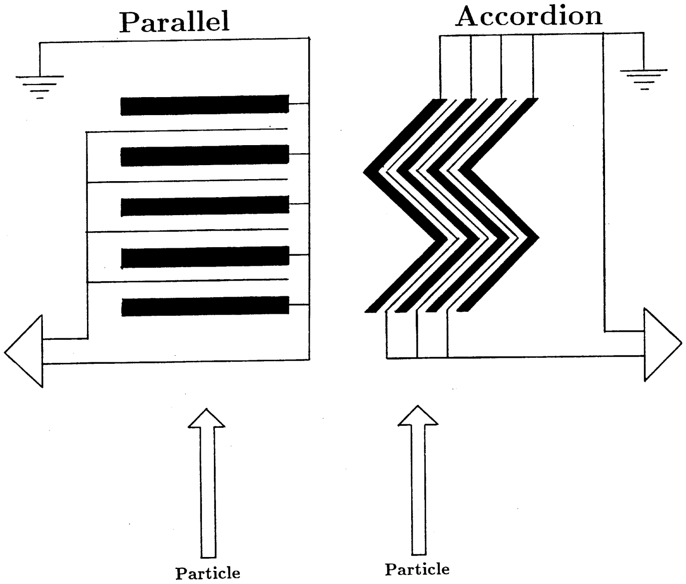

Figure 3.1: Standard and accordion geometry sampling calorimeter concepts.

3.1 The Electromagnetic Cartesian Accordion Prototype

Several accordion EM calorimeter prototypes have been tested [29, 30, 31, 32]. The prototype used in this work is a *cartesian* geometry accordion calorimeter [29, 30]. The absorbers and readout electrodes are separated by a 1.9 mm LAr gap (see figure 3.2). The Pb absorbers are held in place by two horizontal brass supports with accordion shaped grooves shown in figure 3.3.

The readout electrodes are held between neighbouring absorbers by a light honeycomb material of the correct thickness. Printed circuit boards for the calibration system and preamplifiers are mounted on both front and back of the readout electrodes.

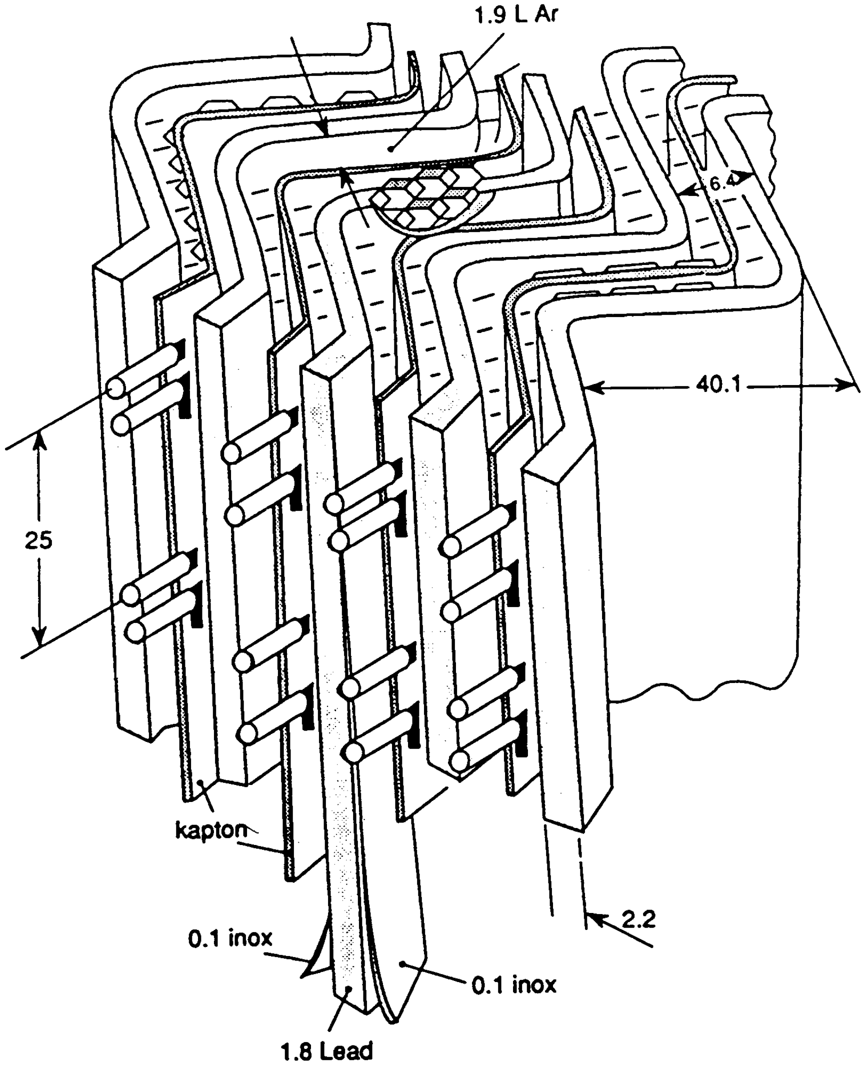

Figure 3.2: An artists view of the accordion calorimeter structure.

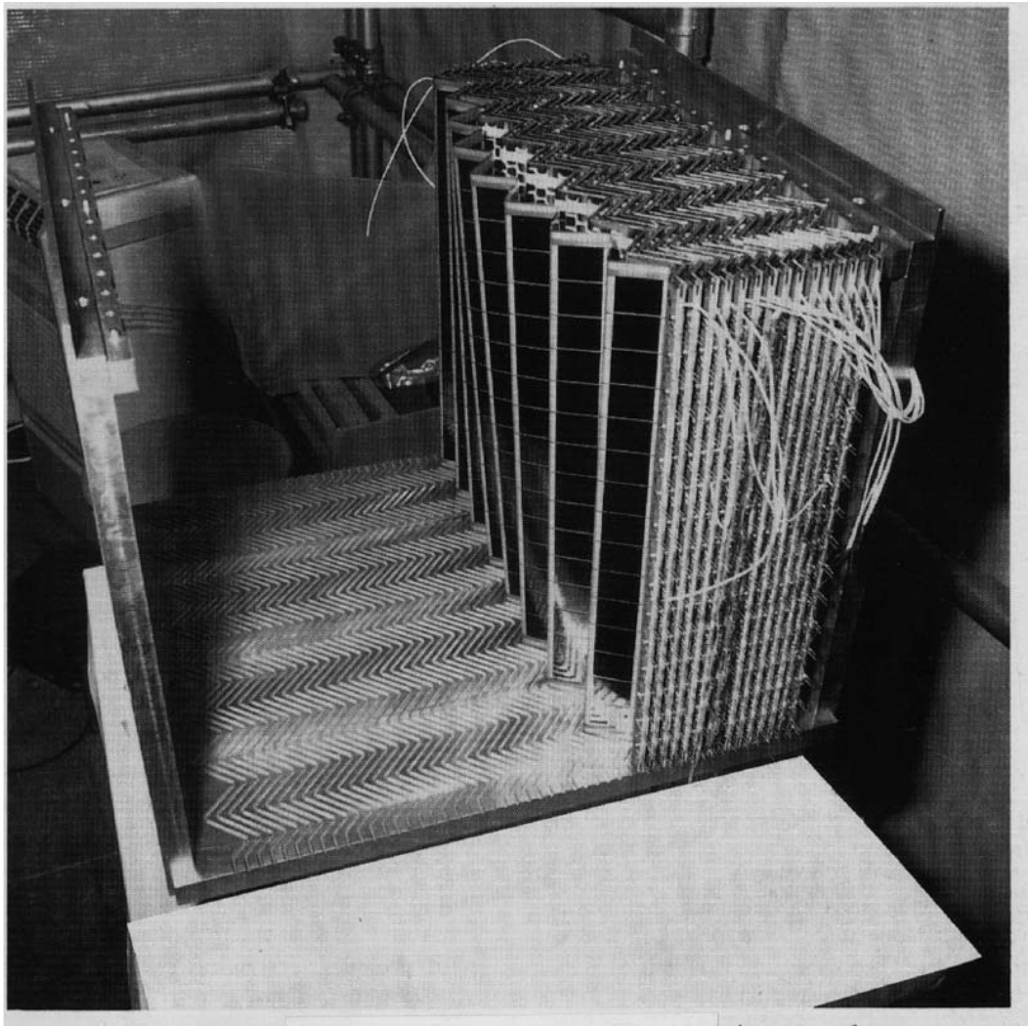

Figure 3.3: The cartesian geometry prototype under construction. A readout electrode is clearly visible. The grooves that hold the absorber in place can also be seen on the bottom plate.

Figure 3.4 shows a plan view of the accordion prototype. The reference system of the prototype is right handed with the Z axis defined along the incident particle direction and the X axis along the accordion folds. It has a section of 30×40 cm^2 and a depth of 45 cm (25.4 X_0). The calorimeter is divided into 12×15 cells in the X×Y direction. In X half the cells are divided longitudinally into two *samplings*, the other half into three samplings.

3.1.1 The absorbers

The absorbers consist of 1.8 mm lead clad in 0.1 mm stainless steel sheets for rigidity and cleanliness of surface. The 16 folds have a pitch of 40.1 mm and an angle of inclination of $\pm 45°$. To keep the electric field inhomogeneities in the LAr gaps to an acceptable level the corners are bent with a 3 mm radius. Each absorber has an unfolded section left at either end to allow for structural and electrical connections.

3.1.2 The electrodes

Each readout electrode is a 0.4 mm thick 3 copper layer printed circuit board made of Kapton, which allows the electrode to be bent in the accordion shape. The front and back ends of each readout electrode have printed circuit connections for the readout and calibration boards. The copper layers of the electrodes are segmented into 24 mm wide longitudinal strips separated by 1 mm which defines the Y granularity. In Z, the longitudinal strips are cut either into two sections to form two 12.7 X_0 *samplings* or in three sections to form samplings of 7.9, 7.9 and 9.6 X_0. The central sampling of the three sampling region is read out at the back of the prototype with a 2 mm wide strip that runs parallel to the third sampling. The inner copper layer of each electrode is capacitively coupled to the outer layers which are held at a high voltage (2 kV) to produce the drift of electrons in the LAr gap. The inner copper layer is DC coupled to a charge preamplifier. The preamplifiers are protected from large signals induced by accidental sparking to the grounded absorber plates by separating the outer copper layer by a special resistive coating on the fold corners.

3.1.3 Front end electronics

The preamplifiers are mounted directly on the front and back of the prototype to allow fast charge transfer from the electrodes to the preamplifiers. Two preamplifier designs were used in this test: silicon J-FETs [33] and gallium arsenide MESFETs [34].

The preamplifiers are mounted on horizontal (X direction) mother boards [29] that gang 3×1 calorimeter cells in $\mathrm{X}\times\mathrm{Y}$ to form a readout cell, which define the 27 mm granularity in X. The resulting readout cell has a total capacitance of $\mathrm{C} = 400$ pF and a total inductance of $\mathrm{L} = 10$ nH. An optimum current rise time of $\tau = 4\sqrt{\mathrm{LC}} = 8$ ns can be achieved provided the preamplifier impedance satisfies the critical damping condition $4\sqrt{\mathrm{LC}}/2\mathrm{C} = 10\,\Omega$ [35]. The input impedances of the preamplifiers are 10 Ω for the GaAs MESFETS and 20 Ω for the Si J-FETS [30].

3.1.4 Signal processing

The intrinsic speed of a LAr sampling calorimeter is restricted by the electron drift velocity v_d in LAr. The v_d in LAr is dependent on the electric field strength up to $\sim 10^4\,\mathrm{V\,cm^{-1}}$ [36] after which saturation takes place. At $10\,\mathrm{kV\,cm^{-1}}$, the operating field of the accordion calorimeter, v_d is approximately $5 \times 10^5\,\mathrm{cm\,s^{-1}}$. This implies total charge collection over the 1.9 mm gap will take a total time of $t_d \sim 400$ ns. This amount of time is clearly too long for a detector at LHC (bunch crossing time of 25 ns). To increase the readout speed use is made of the intrinsic fast rise time ($\sim$ 1 ns) of the drift current in LAr [29]. After the passage of charged particles in a LAr cell, the initial current is proportional to the number of ion pairs produced. The signals from the preamplifiers are brought out of the cryostat using 6 m long $50\,\Omega$ terminated cables via feedthroughs and fed to the bipolar shapers [30]. These fast shapers are specially designed [30] with a peaking time of $\sim$ 20 ns, chosen to minimise the electronic and pile up noise in an LHC calorimeter operating at a beam luminosity of $10^{34}\,\mathrm{cm}^{-2}\mathrm{s}^{-1}$. Integrating this current over a short period of time $t_i \ll t_d$ produces a fast charge signal proportional to the number of ion pairs produced (see figure 3.5(a)). This signal is shaped using a bipolar pulse with characteristic time t_p as shown in figures 3.5(b) and 3.6. The characteristics of the shaped pulse have been studied in detail [35] and its peaking time is approximately equal to $2t_p$ as seen in figure 3.5(c). Fast ($t_p \sim$ 20 ns) bipolar shapers are available and have been tested [30] for use in this readout scheme. The intrinsically low capacitance and inductance of accordion readout cells allows fast charge transfer to properly matched preamplifiers [35].

NO FILE: fig$_a.ps$

Figure 3.4: A top view of a calorimeter prototype segment. The X axis runs from bottom to top of the page and the Z axis runs from left to right. The absorbers (electrodes) are the thick (thin) accordion shaped lines. A readout cell is made up of three ganged electrodes in X.

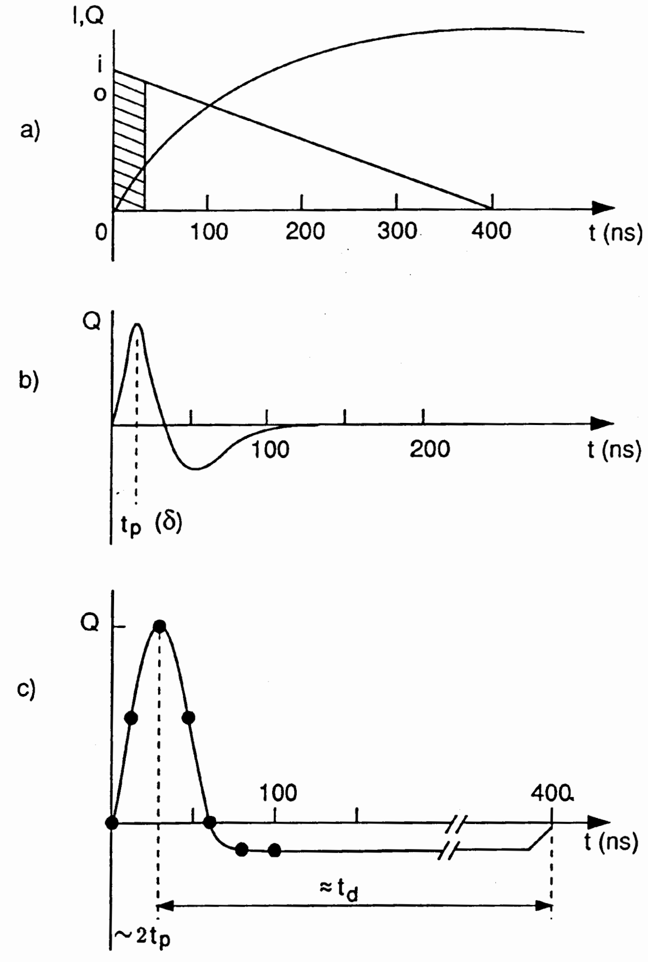

Figure 3.5: (a) Drift current and integrated charge versus time produced by charged particles traversing a LAr cell. The shaded area approximately shows the effective time used to integrate the charge. (b) Response of a bipolar shaper to a short current pulse. (c) Response of the bipolar shaper to the current form in (a). The dots indicate the location of beam crossings if they were to occur every 15 ns.

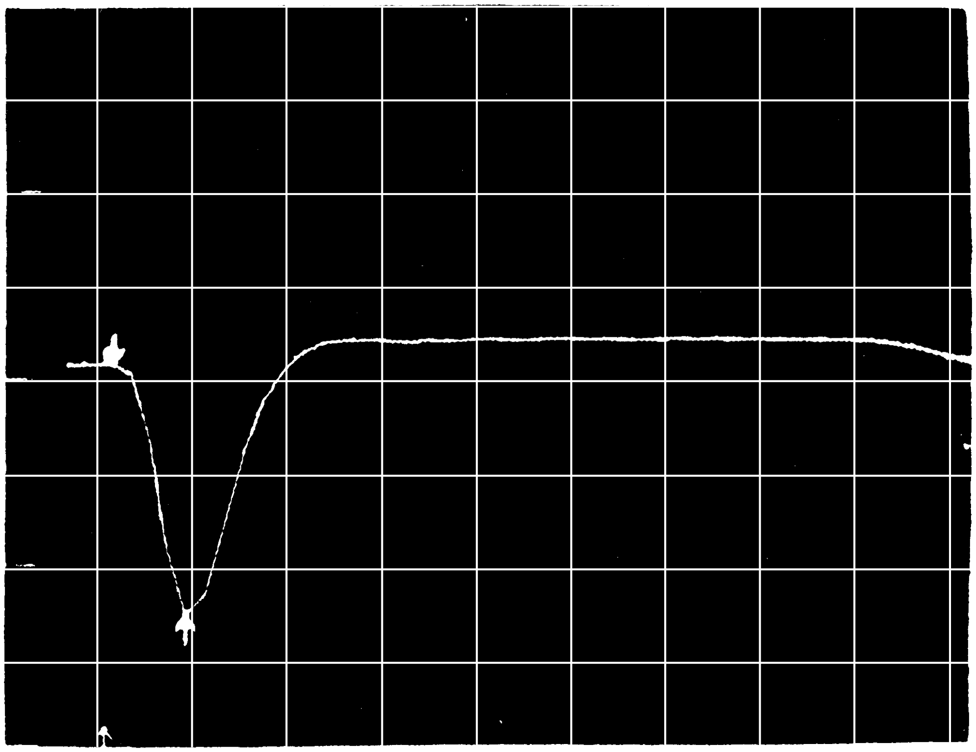

Figure 3.6: Fast shaped signal from a 60 GeV electron hitting one calorimeter cell. The 400 ns drift time is clearly visible (50 mV × 50 ns per square).

The signals from each shaper are sampled by a fast *track and hold* (TH) circuit that tracks the shaper output voltage and, on a timed command from the first level trigger (see section 4.1.2), holds it. Maximum response is achieved if the voltage is held at the peak of the shaped signal as shown in figure 3.5(c). The held voltage is digitised with integrating ADCs that have a variable gate width of $60 - 120$ ns.

The timing of the 'hold' command to the TH circuits needs to be optimised. The optimum delay between the calorimeter signal and the TH is found by injecting a known charge at the preamplifier input and electronically varying the time of the 'hold' command until the maximum response is achieved. The signal must also be timed with respect to the beam as determined by the first level trigger (see section 4.1.2). With an electron beam incident on the calorimeter, the delay between the first level trigger and the TH circuits is varied until the mean of the electron peak is maximum. The timing of the calorimeter was performed at the beginning of the test period.

The energy response of the calorimeter also needs calibration. With the timing set correctly an electronically variable charge is injected at the input of the preamplifiers of every third cell in X×Y through precision test capacitances [30]. The injected charge is shaped with an RC network to simulate the shape of a calorimeter output signal. The calorimeter response as a function of injected charge is fitted with a polynomial function giving a calibration parameters which are stored in the *accordion database.* Runs that perform this calibration are called *test pulse runs.* To fix the absolute energy scale the calorimeter energy response to electrons of a known energy is studied. A calibration constant is introduced to match the mean of the electron peak to the beam energy and is stored in the accordion database. Injecting the charge into every third cell allows the crosstalk between cells to be studied and it is found to be 2% (0.5%) in the vertical (horizontal) direction [30].

The pulse height from each cell when no incident particles are present, or *pedestal*, is studied in *pedestal runs*. The pedestals of each cell are recorded and stored in the accordion database.

3.2 The Pointing Geometry Prototype

The planned ATLAS EM barrel calorimeter uses the same accordion concept as the cartesian prototype affording all the advantages described previously. The absorbers and electrodes are placed around the beam line in full ϕ symmetry. Figure 3.7(a) shows the pointing geometry accordion calorimeter in the r-ϕ plane and figure 3.7(c) shows a perspective view of a module. In the planned full scale ATLAS EM barrel calorimeter the bend angle of the absorber increases with radius to maintain a constant LAr gap.

The granularity in η of the calorimeter is determined by etching divisions on the electrodes that point to the interaction. Longitudinal divisions are etched appropriately, as shown in an r-η view of a readout electrode in figure 3.7(b) where the accordion folds, that run in and out of the page, are not shown. A calorimeter cell is the volume described between the middle of two absorbers in ϕ and by one readout segment in η. These cells can be ganged together in ϕ to form *readout cells.* The planned granularity for ATLAS is $\Delta\eta \times \Delta\phi = 0.025 \times 0.025$.

Readout electronics consisting of a charge sensitive preamplifier for each readout cell are mounted directly on the front (closest to the beam) and back of the detector. This placement of electronic components minimises the amount of dead space in and around the calorimeter needed for readout cabling. This geometry provides full coverage in ϕ and η with minimal dead space. Thus the accordion geometry provides good hermeticity for an LHC detector.

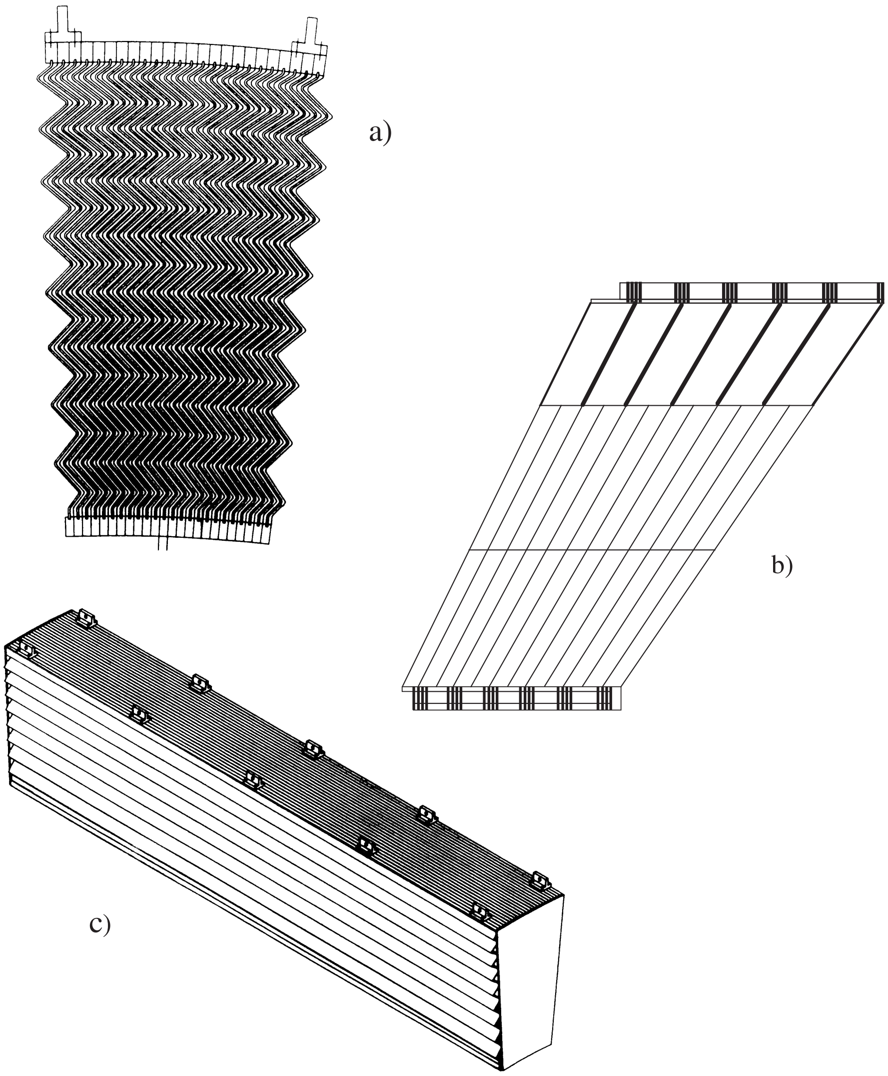

Figure 3.7: (a) Transverse view of a EM prototype module, with radial dimensions of 1.43 to 1.95 m. Note that the angle of the folds vary in order to keep the LAr gap constant. (b) A readout Kapton electrode with segmentation in depth (r)and η shown. (c) Perspective view of a 2 m long module.

Chapter 4

Spatial Reconstruction of Electrons

4.1 Experimental Conditions and Analysis Tools

4.1.1 Test beam setup

The calorimeter prototype was installed the H6 test beam line in the North Area of the CERN SPS in Geneva. Beams of electrons, muons and pions up to a momentum of 205 GeV were available. The particles can be momentum analyzed twice along the line which allows a wide range of particle energies to be produced. To produce electrons of 90 GeV and less a lead target is placed downstream from the first target and momentum analyzer to act as a converter, resulting in a tertiary beam. This tertiary beam then traverses a second analyzer to retain particles of the desired momentum. Above 90 GeV a secondary electron beam is produced by separating electrons from pions in the second analyzer. In the tertiary (secondary) mode the momentum spread ($\frac{\delta P}{P}$) is given to be 0.7% (0.4%). Depending on the configuration of the H6 beam line with other beam lines in the north area the beam could be made of positive or negative particles. The electromagnetic shower characteristics from electrons and positrons of high energy are the same, so that the charge of the particles in the beam does not affect this analysis.

The global coordinate system adopted in the work is right handed with the Z axis running along the incoming particle direction and the accordion folds running along the X axis. The origin of this coordinate system corresponds with the bottom right front face of the calorimeter. When the calorimeter is viewed from the front the X coordinate increases horizontally from right to left and the Y coordinate increases upwards.

The calorimeter was equipped with several types of readout electronics allowing tests of various readout options to be carried out by the RD3 collaboration (see figure 4.1).

The bottom row of 13 cells were equipped with gallium arsenide (GaAs) MESFET preamplifiers [34]. The remaining cells above this row were divided into two main preamplifier regions following the difference in sampling configuration. The first 5 cells from the right edge of the calorimeter, divided into three samplings, were equipped with silicon (Si) J-FET hybrid preamplifiers [33]. The remaining 8 cells configured with two samplings were equipped with GaAs MESFETS. Thus the GaAs and Si regions correspond to the two and three depth sampling regions respectively. Some preamplifiers failed putting a limit on the calorimeter area over which data could be usefully analyzed.

The calorimeter prototype was placed inside the HELIOS [37] experiment cryostat with the HELIOS U-LAr hadronic calorimeter behind to measure electromagnetic shower leakage and hadronic shower energy. The cryostat consists of a 2 cm aluminium outer wall, a 2.7 cm vacuum gap and a 3 mm thick stainless steel inner wall. The liquid argon is cooled using liquid nitrogen circulating in copper coils inside the cryostat. A feedback circuit sensitive to the LAr vapour pressure ensures that the argon is kept in the liquid phase. Between the aluminium wall and the front

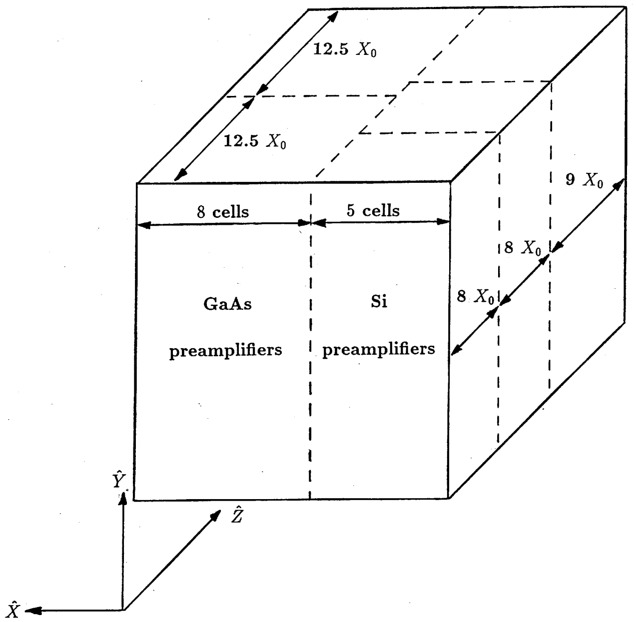

Figure 4.1: Schematic representation of the depth samplings and the preamplifier regions for the cartesian calorimeter prototype.

face of the calorimeter 15 cm of low density foam material was placed to reduce the amount of material (in X_0) in front of the calorimeter. To vary the particles impact on the calorimeter the cryostat is moved by a geared set of electric motors on a rail and pivot system that allows horizontal and vertical movements of ±20 cm and angular movements of $\pm 4^\circ$ about the Y axis. The electric motors are read by an encoder system that allows repeatable positioning of the calorimeter.

The direction of incoming particles is determined by three proportional wire beam chambers [38] upstream from the calorimeter. Each chamber can return an X and Y coordinate for each passing beam particle. The three chambers were placed

7.7 m, 3.8 m and 0.55 m downstream from the calorimeter face to form a telescope. A scintillator beam counter was placed upstream from each of the first and second beam chambers. Downstream from the third beam chamber, close to the calorimeter, two small scintillators defining an area of 3×3 cm^2 readout by fast photomultiplier tubes were placed in the beam and used as an event trigger. Behind the cryostat a large scintillator was placed to tag muon events, see figure 4.2.

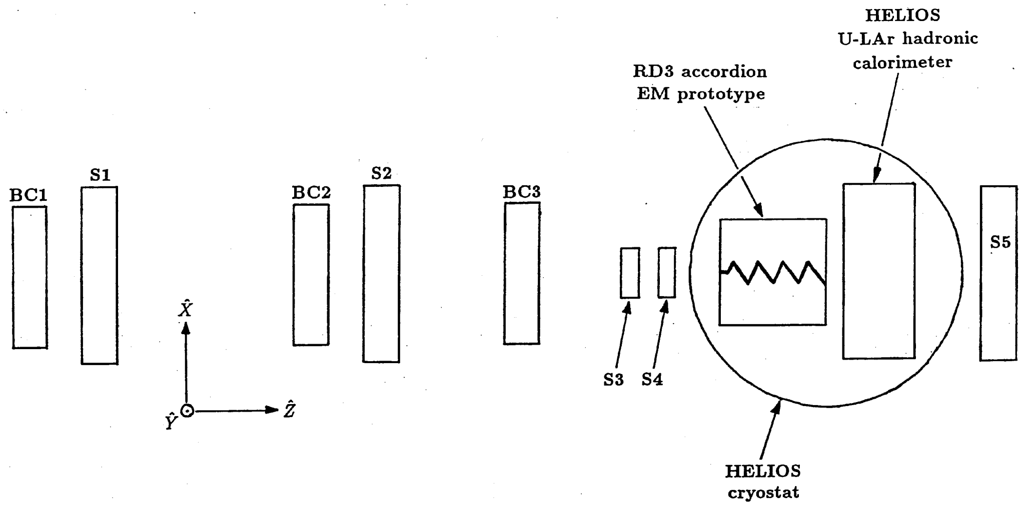

Figure 4.2: The test beam setup for the cartesian prototype test studied. Sn (BCn) refers to scintillator counter (beam chamber) 'n'. The total length is ~ 10 m. Not to scale.

4.1.2 Data taking procedure

Data taking took place in two test beam periods of about 2 weeks each. Within each test beam period many (in the order of 100) data *runs* were taken. Each data run consisted of 5000 to 8000 single particle *events* as read by the data acquisition (DAQ) system. Other run types are calibration and pedestal runs (see section 3.1.4) taken at about 1/10 the frequency of data runs.

Each data run was started and monitored from a Unix work station running the DAQ control programs. During each data run the DAQ system was controlled by a two level trigger. The first level trigger, the fast calorimeter trigger, uses a coincidence signal from the two 3×3 cm^2 counters directly in front of the cryostat to initiate the readout of the data. One counter signal was delayed in order that the trigger was produced by the same counter so that trigger time jitter could be estimated. The small dimensions of these two fast counters defined the beam dimensions on the calorimeter. The second level used information from the large scintillator beam counters placed before and behind the cryostat and from the calorimeter itself. This trigger level either sent a clear signal to the readout system in the case of a bad event or enabled the readout of all the equipment by the DAQ.

Once a correct trigger is received from the counters the energy of all calorimeter cells is read out as counts from the analog to digital converters. The digitized signal from the ADC's are sent to a VME fastbus controller crate that stores the raw data on magnetic tape. Other run dependent quantities, like the beam chamber and scintillator responses, the run number, the encoder values, the particle type and energy, are also stored on tape.

4.1.3 The analysis code

The computer programs used in this study are run in several steps. First, the raw data from the magnetic tapes are read by a program on the CERN VM (or UVIC VM) IBM main frame computer where preliminary selection of events is made. This selection ensures that the correct scintillator signals were received and that the beam chambers were functioning correctly. The calibration and pedestal values for a particular run are read from the accordion database. The energy of each calorimeter cell is determined at this stage by converting the raw ADC counts for each cell into GeV using the appropriate calibration and pedestal values. An important function carried out in this first step is the cell clustering. The clustering procedure gives estimates of the energy and width of a shower as well as the calorimeter reconstructed particle position. This clustering algorithm determines the most energetic cell in each sampling separately. Clusters of cells are formed around these most energetic cells in each sampling. The most energetic cell on the calorimeter front face using all samplings is also determined and similar clusters formed. The X × Y dimensions of these clusters are 3×3, 5×5 and 2×1 respectively.

With the energy and cell number of each cell in the cluster the position, energy and width of a shower is found. The cluster energy is determined by adding the energy of all the cluster cells. The position of a shower is determined by the energy weighted X and Y first moments. The shower width is defined as the second moments.

The output from this program is written in a transportable form and transferred to the HP/Apollo workstation cluster in Victoria where it is analyzed using the standard CERN PAW package [39].

The experimental data are compared to Monte Carlo simulations at various stages of the analysis. These simulations use GEANT [40], a standard CERN detector and electromagnetic shower package. The simulation used in this work describes the cartesian accordion geometry [41] and HELIOS cryostat in detail. The characteristics of simulated electron showers developing in the prototype are studied using this program.

4.1.4 Independent measurement of charged particle impact

A measurement of the particle impact on the calorimeter, independent of calorimeter information, is needed but not readily available. The information available on particle direction is provided by the beam chambers. Each of the three beam chambers located in front of the cryostat, returned an x and y coordinate for every beam particle. The uncertainty on the coordinates for all chambers in the x (y) direction is $257\,\mu$m ($269\,\mu$m). The analysis code used this information and the location of each beam chamber relative to the calorimeter to make a least squares fit. The parameters of this fit are used to extrapolate the particle trajectory to the calorimeter face in the beam chamber coordinate system, giving the *beam chamber impact.* The uncertainty on the beam chamber impact in the x (y) direction is $255\,\mu$m ($260\,\mu$m) (see Appendix A).

The beam chamber coordinate system (x,y) is fixed to the beam line. To vary the beam impact on the calorimeter the calorimeter is moved along with the cryostat and its position is recorded by an encoder system. Accurate survey information relating the calorimeter and encoder reference frame to the beam chamber reference frame is not available. The calorimeter (X,Y) and encoder (m,n) coordinate systems are both fixed to the calorimeter. They are linearly related, with a quadratic term to account for encoder and gear non-linearities. Expressed in the coordinate systems fixed to the calorimeter, the origin of the beam chamber coordinate system is given by $(\mathrm{X_B}, \mathrm{Y_B})$ in the calorimeter coordinate system and is assumed to coincide with the encoder position (m,n) in the encoder coordinate system. We therefore have the relation

$$\mathrm{X_B} = \alpha_\mathrm{x} + \beta_\mathrm{x}\mathrm{m} + \gamma_\mathrm{x}\mathrm{m}^2 \tag{4.1}$$

where α_x, β_x, and γ_x are constants to be determined. A similar relation holds between $\mathrm{Y_B}$ and n with the constants α_y, β_y, and γ_y.

The impact $(\mathrm{X_I}, \mathrm{Y_I})$ of individual particles in the calorimeter reference frame using beam chamber and encoder information only is found by adding the corresponding beam chamber impact (x,y) to $\mathrm{X_B}, \mathrm{Y_B}$

$$\mathrm{X_I} = \alpha_x + \beta_x \mathrm{m} + \gamma_x \mathrm{m}^2 + \mathrm{x}. \tag{4.2}$$

The constants α, β, and γ can be obtained if a representative set of corresponding coordinates (X,Y) and (x,y) are known.

The calorimeter reconstructed particle impact position in the calorimeter coordinate system $(\mathrm{X_C}, \mathrm{Y_C})$ is obtained by calculating the energy weighted centroid of the corresponding calorimeter cell cluster. It is subject to clustering effects, in particular for impacts near cell edges. The calorimeter reconstructed position shows a systematic break at cell edges and this effect is understood and can be explained.

All impacts within a hit cell are considered. The centroid calculation is biased towards the middle of the cluster as the impact position within the cell approaches an edge. At the edge of a cell the reconstructed position is biased away from the edge. As the cluster size is increased more energy information is used in the centroid calculation and the effect decreases. Figure 4.3 shows two profiles; on the left a profile of the beam impact on the face of the calorimeter in the beam chamber reference frame; on the right the corresponding 3 × 3 cell cluster calorimeter reconstructed position using the first sampling. The histogram on the right shows the break occurring slightly to the right of the cell edge. From this effect, the coordinate $(\mathrm{X_C}, \mathrm{Y_C})$ corresponding to a cell edge can be found which allows, with the readily available corresponding beam chamber coordinates (x,y), the computation of the constants α, β, and γ.

A series of data runs that cover the calorimeter face in both X and Y directions

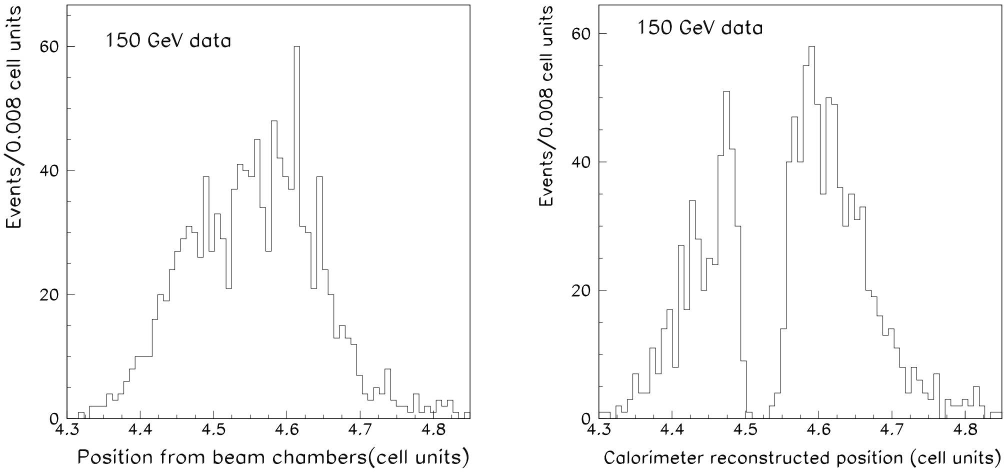

Figure 4.3: Particle position as returned from the beam chambers (left) and the calorimeter reconstructed position using a 3×3 cell cluster in all samplings. Each plot uses the same data and the clustering break is clearly visible at the edge of the cell (indicated by the half integer value).

are selected. An electron sample is selected from each run as outlined in section 4.2. For each run the beam chamber impact is plotted as a function of the calorimeter reconstructed position as shown in figure 4.4. The break in the clustered position is assumed to coincide with a cell edge and is clearly visible as a gap in the distribution. Thus the cell edge is identified in both the beam chamber and calorimeter reference frames. By repeating the procedure for all cell edges a representative set of coordinates X_C, Y_C and x,y are found for all regions of the calorimeter, allowing the constants α, β, and γ to be determined. These constants are found for each region (two sampling and three sampling regions) and each direction (X,Y) on the calorimeter face. The RMS of the residuals of this procedure are shown in table 4.1. For every event an impact point predicted by the encoders and the beam chambers

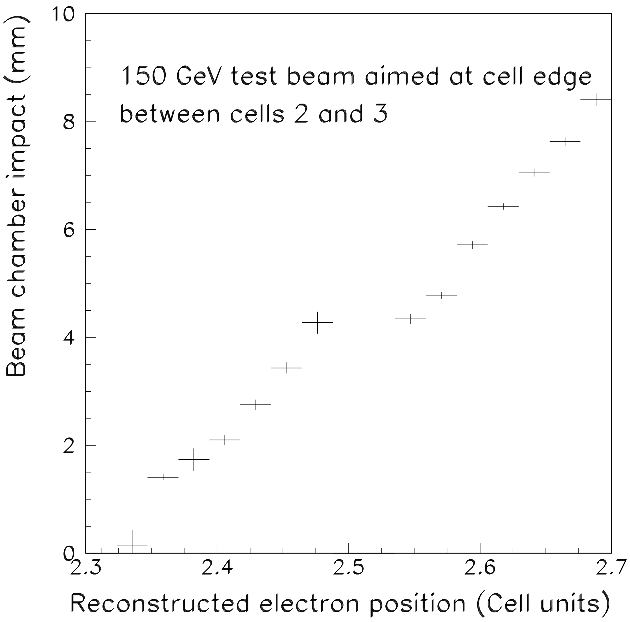

Figure 4.4: The beam chamber impact versus calorimeter reconstructed position using a 3 × 3 cell cluster in the first sampling. The clustering break is seen and matched to a beam chamber value of ∼ 4.5 mm.

called *impact* can then be found.

4.2 The Electron Sample

The calorimeter energy response to a typical 150 GeV electron beam can be seen in figure 4.5. The abscissa shows the energy in a 3 × 3 cell cluster using all samplings, E(3 × 3), calibrated so that the mean of the electron peak corresponds to the beam energy. In figure 4.5 three populations of particles in the beam can be seen: muons deposit small amounts of energy through ionization and populate the sharp low

Table 4.1: The RMS of the residuals of the impact calculation, which are a measure of the error in the impact calculation.

Region	Direction	RMS Residual (μm)
Three sampling	X	373
	Y	469
Two sampling	X	778
	Y	425

energy peak; charged pions initiate hadronic showers not contained in the calorimeter and populate the very broad distribution centered around 60 GeV; electromagnetic showers from electrons are well sampled by the electromagnetic calorimeter and populate the peak at 150 GeV.

To study the position and angular reconstruction of electrons an electron sample is extracted from the test beam data. The first selection method (or *cut*) to obtain a good quality electron sample consists of excluding all the events to the left of the electron peak as proposed by figure 4.5 in the case of a 150 GeV beam. This energy selected sample is now referred to as an *electron sample*. This is a useful cut since muons are completely rejected as well as almost all charged pions. Yet charged pion contamination still remains under the electron peak. This can be estimated by extrapolating the pion distribution under the electron peak. But the pion distribution is small and uncertain close to the electron peak leading to a poor estimation of the pion contamination in the electron sample.

Another method of finding the pion contamination using a pair of uncorrelated cuts is employed. These uncorrelated cuts must be able to reject pions while retaining electrons with a high efficiency. In an attempt to ensure that the cuts be uncorrelated, use is made of different aspects of the electromagnetic shower shape:

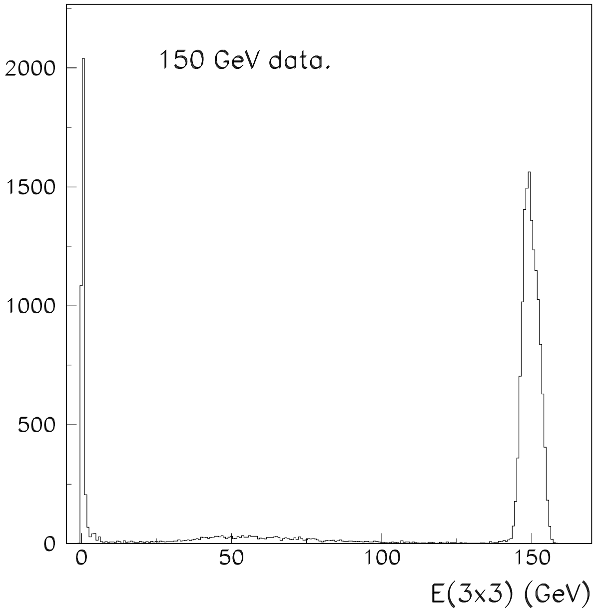

Figure 4.5: Energy response of the calorimeter to a 150 GeV electron beam using a 3×3 cell cluster and all samplings. The energy is calibrated so that the mean of the electron peak corresponds with the beam energy.

the longitudinal and the lateral shower sizes.

The longitudinal cut selects events in the three sampling region as electrons if the cluster energy in the first sampling, $E_1(3 \times 3)$, is greater than the cluster energy in the third sampling, $E_3(3 \times 3)$. For events in the two sampling region the criterion is $E_1(3 \times 3) > E_2(3 \times 3)$. This cut makes use of the difference in the characteristic lengths governing the electromagnetic (X_0) and hadronic (λ_{int}) shower processes and will favour electrons. The prototype has a depth of 25.4 X_0 which ensures electromagnetic showers produces by electrons of up to many hundreds of GeV to be practically fully contained in the calorimeter prototype. An electron impinging on the calorimeter promptly showers electromagnetically, depositing a significant amount of energy in the first sampling which is 7.9 X_0 deep. An electron shower contained in the calorimeter always deposits less energy in the last sampling than in the other samplings. In comparison, the prototype has a hadronic interaction length of $\sim 1\ \lambda_{\rm int}$. An incident charged pion is likely to interact with one of the nuclei in the calorimeter and to start a hadronic shower. This hadronic process will produce prompt meson components that interact electromagnetically (π^0's and η's). Approximately one third of the total number of mesons produced are of this nature. Thus the amount of energy deposited in the calorimeter on average grows in depth with large fluctuations. The energy deposited in the third sampling of the calorimeter by a charged pion shower will be, on average, greater than in the other samplings. The longitudinal cut therefore disfavours charged pions.

The lateral cut selects events as electrons if $0.945 < E_1(3\times3)/E_1(5\times5) < 1.0$, where $E_1(3\times3)$ and $E_1(5\times5)$ are the 3×3 and 5×5 cell cluster energy in the first sampling respectively. The fraction $E_1(3\times3)/E_1(5\times5)$ is clearly sensitive to the lateral shape of the shower. The cut values used were determined from visual inspection of the $E_1(3\times3)/E_1(5\times5)$ distributions for electrons and pion samples near the electron peak. The lateral cut, as for the longitudinal cut, makes use of the differences between high energy hadronic and electromagnetic showers since a hadronic shower is generally wider than an electromagnetic shower of the same energy. Thus the lateral cut favours electrons.

The correlation of the two cuts was calculated and found to be $\leq 5\%$ (details in Appendix B). These cuts were then applied to an electron sample. Let N be the number of events in the electron sample. Then

$$N = S + B\,, \tag{4.3}$$

where S and B are the signal (electrons) and background (charged pions) contents of the electron sample.

After applying the longitudinal cut to the electron sample we have

$$\mathrm{N}_1 = \varepsilon_1 \mathrm{S} + \frac{\mathrm{B}}{\mathrm{R}_1}, \tag{4.4}$$

where N_1 is the number of events left after the cut, ε_1 and R_1 are the electron efficiency and the charged pion rejection of the cut respectively.

Similarly applying the lateral cut we have

$$\mathrm{N}_2 = \varepsilon_2 \mathrm{S} + \frac{\mathrm{B}}{\mathrm{R}_2}. \tag{4.5}$$

The pion rejection of a cut applied to the electron sample can be obtained by studying the pion rejection of the same cut applied to a *pion sample* as shown in figure 4.6. A pure pion sample is obtained by retaining events between the muon and electron peaks. The pion rejections used above were determined in a pion sample close to the electron peak. R_1 and R_2 are assumed to apply to pions within the electron peak.

Equations 4.3, 4.4 and 4.5 contain four unknowns: S, B, ε_1, and ε_2. Another equation is needed to solve the system. Applying the cuts simultaneously, we get

$$\mathrm{N}_{12} = \varepsilon_{12} \mathrm{S} + \frac{\mathrm{B}}{\mathrm{R}_{12}}. \tag{4.6}$$

Since the cuts are uncorrelated we have

$$\varepsilon_{12} = \varepsilon_1 \varepsilon_2 ,$$

$$\mathrm{R}_{12} = \mathrm{R}_1 \mathrm{R}_2 .$$

Equations 4.3, 4.4, 4.5 and 4.6 can be solved for the four unknowns S, B, ε_1, and ε_2 for a given electron data sample (see Appendix B). For all electron samples considered in this analysis, the contamination $\frac{B}{N}$ is found to be less than 3% and is neglected.

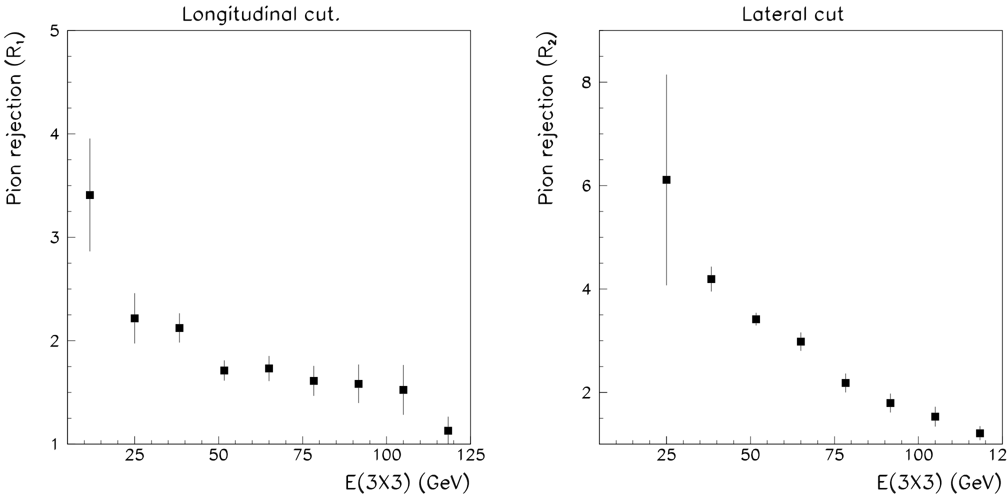

Figure 4.6: Pion rejection factors for the longitudinal and lateral cuts as a function of the pion energy in a 3 cluster using all samplings. The rejection factor falls with increasing energy because the EM component of the hadronic shower increases.

4.3 Position Reconstruction

The primary purpose of the accordion EM calorimeter is to measure the energy of EM showers. Its high granularity also allows accurate position information to be obtained. The energy weighted barycentre of a cluster gives its calorimeter reconstructed position (X_C, Y_C) in the calorimeter coordinate system. The calorimeter reconstructed position (X_C, Y_C) is compared to the particle impact (X_I, Y_I) for many events. The width of the resulting distribution gives the position resolution.

The simulated distributions of electron position, using impact versus a 3×3 cell cluster and all samplings, are shown in figure 4.7. On each plot a diagonal line shows the ideal case when the impact and calorimeter reconstructed position agree exactly. The general features of the curves in figure 4.7 are different, reflecting the

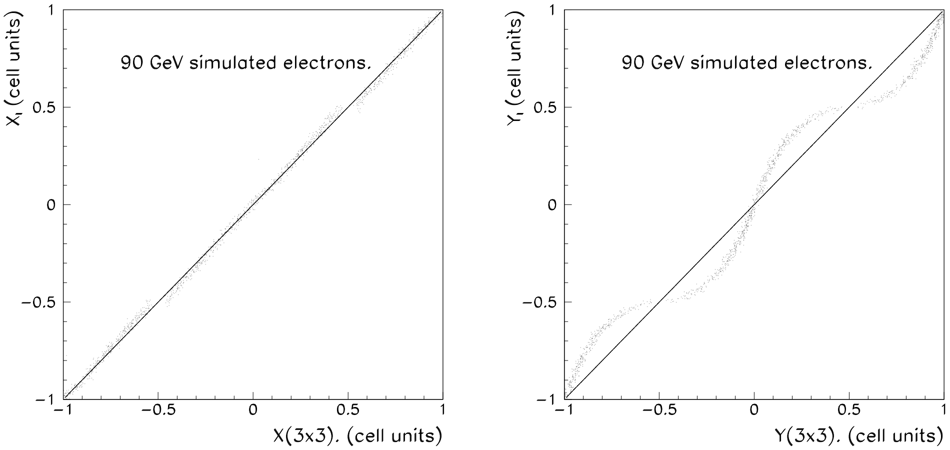

Figure 4.7: The simulated position reconstruction across the face of a calorimeter cell. The figure on the left (right) shows the impact versus simulated calorimeter reconstructed electron position in the X (Y) direction. Cell edges occur at the half integer values.

different calorimeter geometry in the X and Y directions. The accordion structure plays no part in the Y direction behaviour as the calorimeter is effectively segmented into simple cells.

The Y direction curve is understood by considering the cell size and the lateral electromagnetic shower size. The steep centre region (corresponding to -1, 0, 1 position in cell units) shows the decreased position reconstruction accuracy when almost all of the shower energy is contained in the central cell of the cluster. As the electron impacts closer to the cell edge the position reconstruction accuracy improves due to an increased shower energy sharing between neighbouring cluster cells.

In the X direction the accordion geometry influences the calorimeter reconstructed electron position. The lateral folds of the accordion allow neighbouring cells to gather a larger proportion of shower energy than in the Y direction case. Therefore the energy is more evenly spread throughout the cluster in X and position reconstruction is more accurate across a whole cell. In both the X and Y cases the clustering effect at the cell edges can be seen. As the electron impact approaches the cell edge the distribution curves away from the ideal line and the calorimeter reconstructed position breaks at the edge.

Experimentally this study necessitates electron impacts covering a whole cell. Unfortunately the beams incident in all data runs do not cover a whole cell in X or in Y in a single run. Data from many runs taken at different but close locations on the calorimeter therefore have to be merged to cover a cell in one data sample. An electron sample is extracted from each run as outlined in section 4.2 and electron events in the cell to be studied are retained.

Runs to be merged are selected carefully to reduce the following systematic errors:

- The calibration of the calorimeter cells differs over time and merging data with significantly differing calibration degrades the overall response of the sample;
- The response of some cells varies over time. The output signals of some channels were seen to weaken, improve or entirely cease over time. A weak or dead channel in a cluster significantly affects the position reconstruction;
- Errors in the encoder and gear drive mechanism add up to produce impact prediction errors.

A general strategy to minimize the first systematic error, related to calibration, is to minimize the time difference between merged runs. The difference in response of the cells due to calibration can be estimated by observing the energy response of certain *reference cells* in each region of the calorimeter. A reference cell is a cell in the middle of a problem free 5 × 5 cell cluster. Frequent data runs are made on these cells to monitor the calorimeter performance over time. The energy response of the reference cells was studied and the variation of response over the data taking period was found to be negligible for this position reconstruction study.

The second systematic error related to the degraded response of cells over time is minimized by avoiding such cells. A cell that showed weak or no response is not included in any clusters. Requiring that the cluster centre is at least two cells distant from a dead or weak cell is the method used to exclude such a cell from this study.

The third source of systematic error related to the encoder and gear drive mechanism is considered separately for the X and Y directions in the sections below.

4.3.1 Position reconstruction in the Y direction

The calorimeter position reconstruction over a whole cell in the Y direction is considered first. Figure 4.8 shows the relationship between the electron impact in the Y direction ($\mathrm{Y_I}$) and the calorimeter reconstructed position $\mathrm{Y_C}$ of a typical cell. The experimental data and Monte Carlo predictions agree well as can be seen by comparing figures 4.7 and 4.8. Figure 4.8 clearly shows the clustering effect at the cell edge, referred to in section 4.1.4, that coincides well with the cell edge predicted by $\mathrm{Y_I}$. This observation allows direct merging of runs that cover different areas of a cell. The general electron population of each cell can be seen in figure 4.8. Each cell is well populated in the centre and at the edges.

The curve in figure 4.8, replotted as $\mathrm{Y}(3 \times 3)$ versus $\mathrm{Y_I}$, is well approximated by a tangent function and fitted with

$$\mathrm{Y}(3 \times 3) = a + b * tan(c * (\mathrm{Y_I} - d)) \tag{4.7}$$

where a, b, c and d are constants found independently for each cell studied. The

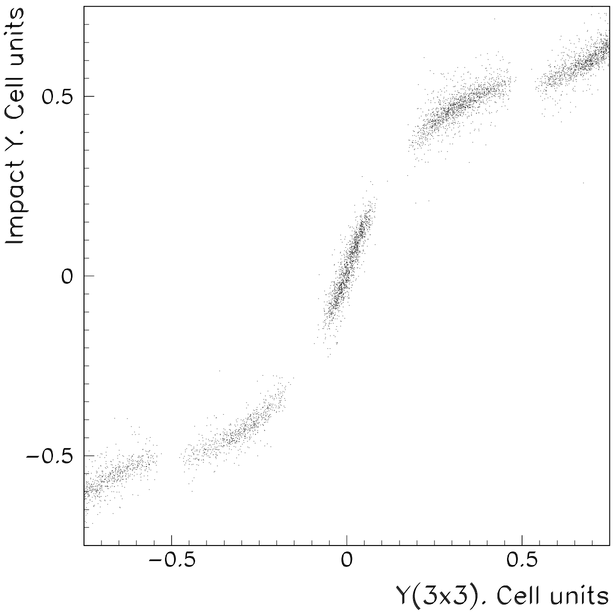

Figure 4.8: Impact in the Y direction versus calorimeter reconstructed position using a 3 × 3 cell cluster in all samplings. The cell centre (edges) corresponds to 0 (±0.5) on both axes. The clustering effect is clearly visible as a break in the curve at the cell edges along the abscissa. The breaks near 0 are due to a lack of experimental data at the corresponding impacts.

function is then inverted and a corrected calorimeter reconstructed position, $Y'(3 \times 3)$, is found. A global fit between cells could not be found without seriously impairing the position reconstruction performance, pointing to possible calibration problems.

The calorimeter position reconstruction performance is found by observing the distribution of $Y'(3 \times 3) - Y_I$. The calorimeter position resolution in the Y direction is given by the width of this distribution after the impact uncertainty is unfolded.

The calorimeter face is covered only by 120 and 150 GeV electron data. The

Table 4.2: Experimental position resolution over a cell width in the Y direction. The first error is statistical, the second is systematic.

Region	Electron energy (GeV)	$\sigma_{Y'_1(3\times3)}$ (μm)
Three sampling	150	$598 \pm 12 \pm 42$
	120	$626 \pm 13 \pm 103$
Two sampling	150	$463 \pm 12 \pm 61$
	120	no data available
Previous RD3 result	122	570 ± 25

position resolutions obtained in Y using a 3×3 cell cluster in the first sampling only, $Y'_1(3 \times 3)$, are summarised in table 4.2. Position resolution improves with energy as expected. The 150 GeV data results show that the deeper (12.7 X_0) first sampling of the two sampling region gives a better position resolution than the shallower (7.9 X_0) first sampling in the three sampling region. This result is expected since a deeper first sampling contains more of the shower energy resulting in a better position resolution.

The dependence on energy of position resolution over a whole cell cannot be checked in the Y direction. The data taken in the two test beam periods did not include full cell scans in the Y direction at different energies. Also the general energy dependence of position resolution in the Y direction cannot be checked with the data present. The runs taken at 20, 60 and 90 GeV only impact the edge of a cell in the Y direction. The position resolutions found from these runs are dominated by the clustering edge effect and are not indicative of the calorimeter performance.

The published result [29] for the Y direction calorimeter position resolution is shown in table 4.2. It is better than the one found in this analysis because the data used in [29] has impacts in the regions between the edges and centre of the cell which have inherently superior position reconstruction performance as outlined briefly in section 4.3.

4.3.2 Position reconstruction in the X direction

We now consider the position reconstruction of electrons over one cell in the X direction. Each cell is covered by merging several runs that partially cover the cell width. An electron sample is extracted from each run and the electron events in the cell to be studied are retained. The X direction analysis considers the position reconstruction in both the first and second samplings using a 3×3 cell cluster. The third sampling of the three sampling region is not considered due to the large fluctuations in the width of showers at such a depth.

In the X direction the accuracy of the impact measurement is checked for each run. Possible encoder and drive gear errors are studied by comparing the difference of $X(3 \times 3)$ and impact for each run across the face of the cell. $X(3 \times 3)$ is chosen for this comparison since the most accurate calorimeter position reconstruction is obtained using all samplings of the calorimeter. $X(3 \times 3)$ is assumed constant over the face of a cell and flat within each beam spot as indicated in previous Monte Carlo studies [41]. The behaviour of $X(3 \times 3) - X_I$ over the face of the cell can be seen in figure 4.9. The different symbols on the figure correspond to different runs. $X(3 \times 3)$ is experimentally found to be flat within each run except close to the cell edges where the clustering effect dominates. In figure 4.9 $X(3 \times 3) - X_I$ is seen to jump from run to run, pointing to a run dependent systematic effect likely to be caused by the impact measurement dependence on encoder values read from the drive gears that position the calorimeter for each run. Since the encoder values passed to the analysis code are identically treated to calculate impact from run to run, the gearing that drives the calorimeter and cryostat in the X direction

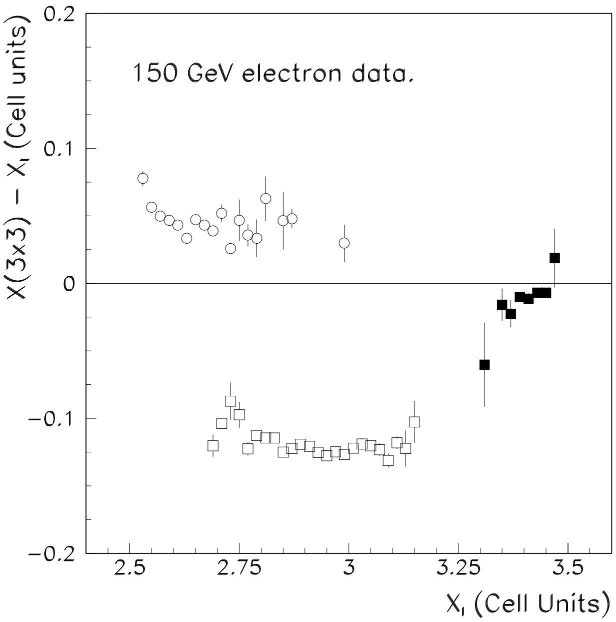

Figure 4.9: Calorimeter reconstructed position using a 3×3 cell cluster in all samplings minus the impact in X versus the impact in X. The symbols correspond to different individual runs. The difference between runs is clearly visible. $X(3 \times 3)$ is experimentally flat within each run.

is probably at fault. This systematic effect has to be corrected if runs are to be merged successfully.

To reduce this systematic effect the impact is corrected on a run to run basis by adding the average value of $X(3 \times 3) - X_I$ to the impact measurement. This new impact is referred to as the *corrected impact* or X_I'. Figure 4.10 shows X_I' versus $X(3 \times 3)$ for several merged runs in a cell. The corrected impact can be seen to behave as predicted by simulations (see figures 4.7 and 4.10). The three distinct populations in figure 4.10 represent a typical beam coverage of a cell in the

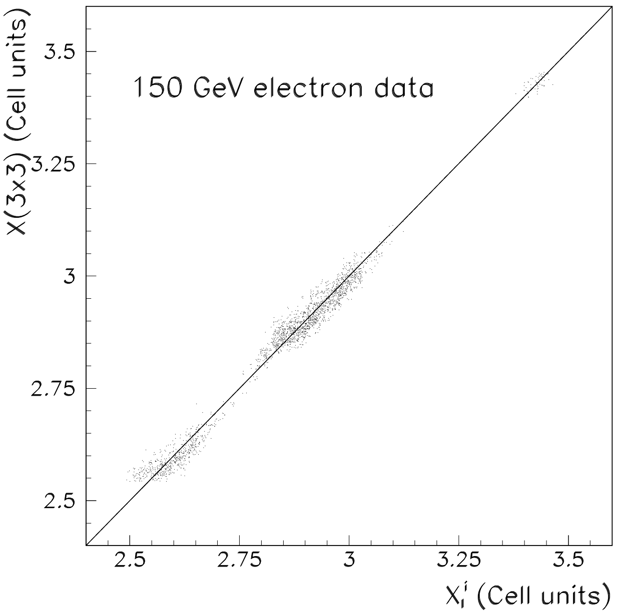

Figure 4.10: Calorimeter reconstructed position using a 3 × 3 cell cluster in all samplings versus the corrected impact in X of 120 GeV electrons. The diagonal line represents ideal reconstruction. The three distinct populations in the figure are representative of the typical level of coverage of a cell.

X direction.

The calorimeter position reconstruction in X differs strongly from the one in Y (see figure 4.7). The effect of the accordion folds on the calorimeter reconstructed position in X deserves close investigation. The number of accordion folds used to form the first sampling has an effect on the average calorimeter reconstructed position in X in the first sampling, as was shown in previous Monte Carlo work [41]. These simulations show that using 5 (16) folds in the first sampling leads to an average difference between the calorimeter reconstructed position and the impact of ~ 1.2 mm (< 0.1 mm) (*position offset*); using more shower energy increases the average position reconstruction accuracy and decreases the position offset.

An *average* offset is irrelevant when position resolution is studied, but the calorimeter reconstructed position as a function of impact within a cell is crucial. The dependence of the calorimeter reconstructed position of electrons on the impact point within a cell was studied using Monte Carlo simulations. The difference between the calorimeter reconstructed position of electrons using a 3 × 3 cluster in the first sampling and the impact is defined as the *position offset.* The position offset can be plotted as a function of impact using

$$\mathrm{X}_1(3 \times 3)\ -\ \mathrm{X}'_{\mathrm{I}} \text{ versus } \mathrm{X}'_{\mathrm{I}} \tag{4.8}$$

for various electron energies and angles of incidence. This position offset is understood to be an effect of the accordion geometry in the X direction and the electron shower shape. Within a sampling, the position reconstruction will be biased mainly by the accordion structure present at the depth of maximum energy deposition. As the impact point moves laterally within a cell, the accordion structure changes at this depth producing a non-uniform position bias. Systematic position offsets as a function of impact were found in simulation studies of electrons from 30 to 200 GeV and angles of incidence up to ±2.3°.

The position offset as a function of impact does not depend on energy, as shown in figure 4.11, but are seen to vary within about 0.05 cell units (~ 3 mm) for different impacts.

The position offset depends on the electron angle of incidence. Figure 4.12 shows the position offset as a function of impact for three closely separated angles. The amplitude and shape of each curve can be seen to vary as a function of electron angle of incidence over a ±20 mrad range. This dependence on angle of incidence

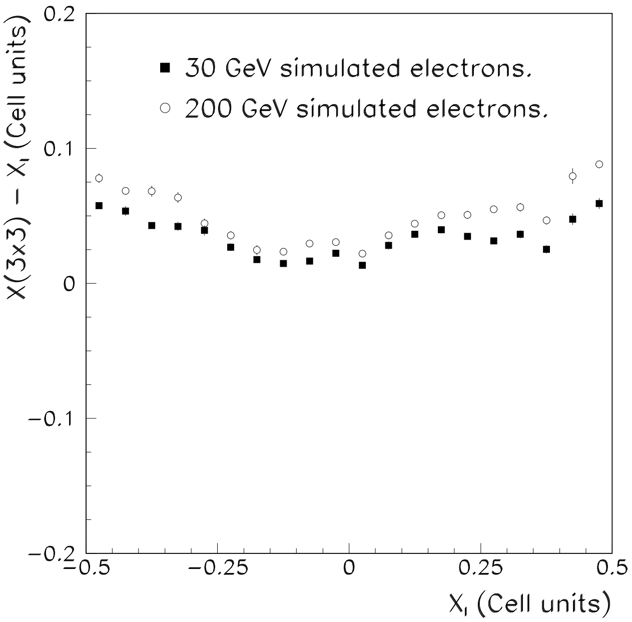

Figure 4.11: Simulated $X_1(3 \times 3)$ minus X_I versus X_I for two energies that encompass the available experimental range. The amplitude and shape of the distributions are seen to be similar for these energies. All intermediate energies show similar shapes.

has serious consequences for the analysis of the test beam data.

Figure 4.13 shows the comparison between the position offsets in experimental data and in Monte Carlo simulations obtained using equation 4.8. The experimental and Monte Carlo results agree across parts of the cell width (see figure 4.13). The run impacting the centre of the cell agrees well with simulation, in contrast to the cell edge runs where the clustering effect dominates. In the simulation the impact is well known whereas the test beam impact is corrected on a run to run basis with possible residuals (note the vertical scale of figure 4.13).

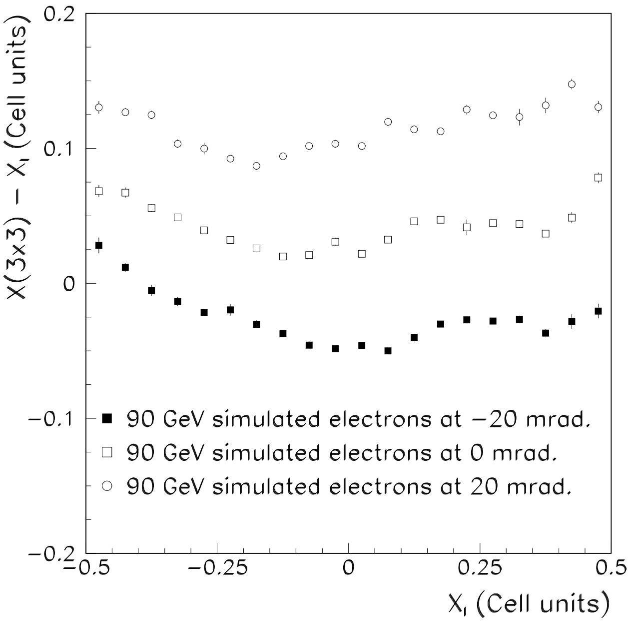

Figure 4.12: Simulated $X_1(3\times3)$ minus X_I versus X_I for three angles of incidence. The amplitude and shape of the distributions can be seen to vary significantly over this angular range.

To verify that the position offsets are really a feature of the accordion calorimeter another quantity is studied. For both Monte Carlo and test beam data, $X(3\times3)$ is substituted for X'_I and

$$X_1(3\times3)\;-\;X(3\times3)\text{ versus }X(3\times3) \tag{4.9}$$

is studied (see figure 4.14). By using $X(3\times3)$ in place of X'_I the errors in the run to run impact correction are removed.

Test beam data coincide with simulated electrons with an angle of incidence of 30 and 40 mrad (see figure 4.14). This agreement suggests that the beam is oriented

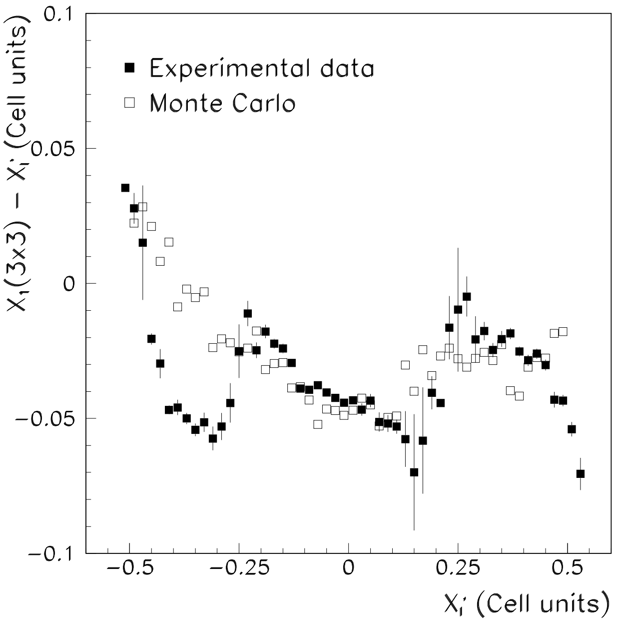

Figure 4.13: $X_1(3\times3)$ minus corrected impact versus corrected impact for both data and Monte Carlo across a single cell. The experimental data exhibits a threefold pattern corresponding to the three runs used to cover the cell and are caused by imperfect impact corrections. The Monte Carlo results are smooth across the cell.

at $\sim 2^\circ$ with respect to a line normal to the calorimeter face. Given the size of the effects, this agreement is impressive.

These position offset patterns were checked in both the two and three sampling regions in the first and second samplings. The position offsets are systematic and due to the calorimeter geometry in the X direction and in principle can be corrected for. Substituting $X(3\times3)$ for X_I in the experimental study of position resolution is not valid because of the correlation between $X(3\times3)$ and $X_1(3\times3)$. Therefore all experimental position offsets are studied with respect to X'_I.

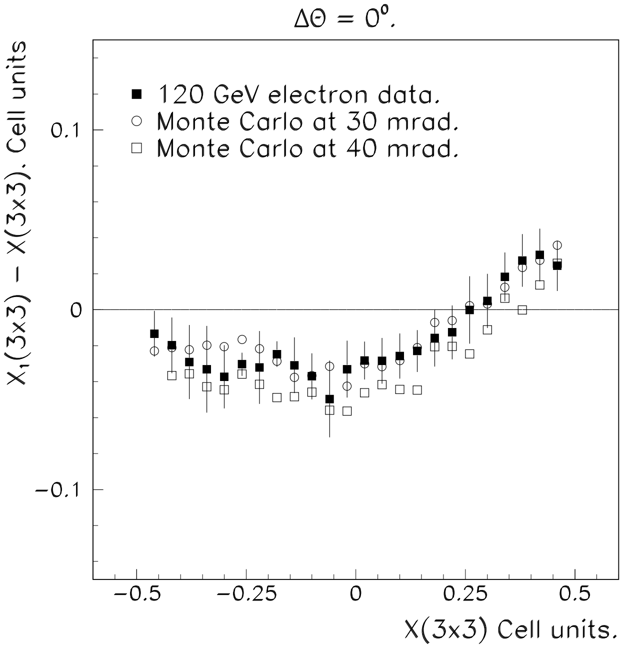

Figure 4.14: $X_1(3 \times 3)-X(3 \times 3)$ versus $X(3 \times 3)$ across a cell width in X for both experimental data (statistical errors shown) and Monte Carlo (errors not shown, smaller than the experimental runs).

The experimental position offsets of figure 4.13 do not agree well when observed over all cells. Differences in impact error for each run and subsequent correction residual errors account for this discrepancy. This implies that a global systematic position offset correction using the impact cannot be applied, which shows the importance of a reliable knowledge of the impact. Instead, the position offset corrections are applied to each cell using the calorimeter electron position data.

Offset corrections are performed in two stages. Firstly, a position correction for each cell are created using the bin contents of figure 4.13, forming a piece-wise continuous function. Secondly, the correction values are subtracted from the calorimeter reconstructed position on an event by event basis, producing the corrected calorimeter reconstructed position.

Figure 4.15 shows the corrected and uncorrected calorimeter reconstructed position using a 3×3 cell cluster in the first sampling minus corrected impact $X_1(3 \times 3) - X_I'$. The corrected distribution in figure 4.15 is narrower than in the uncorrected case. This behaviour is noted for all cells studied. The *corrected calorimeter posi-*

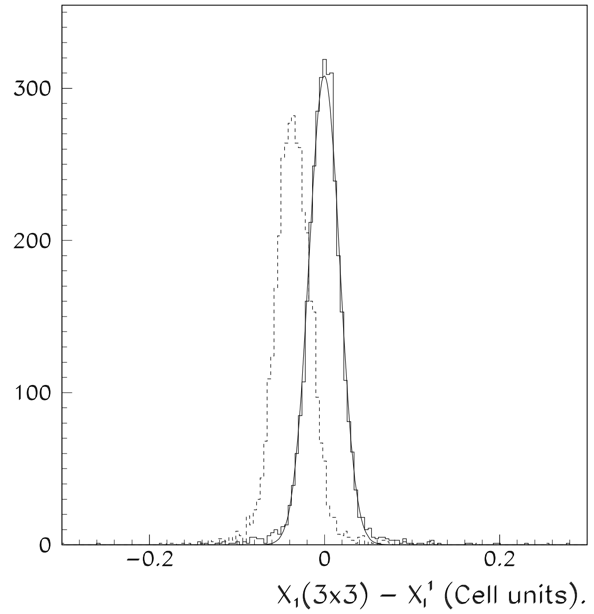

Figure 4.15: $X_1(3 \times 3)$ minus X_I' for 150 GeV electrons across a cell width in X. Position offset corrected (uncorrected) experimental data are shown as the solid (dashed) histogram and fit curve. After unfolding the beam impact uncertainty the corrected (uncorrected) calorimeter position resolution is 224 ± 3 μm (360 ± 4 μm).

Table 4.3: Position resolution results over a whole cell in X for the first sampling in both calorimeter regions. The first error is statistical, the second is systematic.

Region	Electron energy (GeV)	$\sigma_{\mathrm{x}_1(3\times3)}$ (μm)	$\sigma_{\mathrm{x}'_1(3\times3)}$ (μm)
Three sampling	150	$766 \pm 9 \pm 123$	$544 \pm 6 \pm 33$
	120	$906 \pm 7 \pm 27$	$509 \pm 4 \pm 31$
Two sampling	150	$556 \pm 7 \pm 22$	$451 \pm 5 \pm 27$
	120	no data available	

Table 4.4: Position resolution results over a whole cell in X for the second sampling in both calorimeter regions. The first error is statistical, the second is systematic.

Region	Electron energy (GeV)	$\sigma_{\mathrm{x}_2(3\times3)}$ (μm)	$\sigma_{\mathrm{x}'_2(3\times3)}$ (μm)
Three sampling	150	$1203 \pm 15 \pm 193$	$749 \pm 9 \pm 127$
	120	$1293 \pm 10 \pm 26$	$947 \pm 8 \pm 95$
Two sampling	150	$1193 \pm 13 \pm 48$	$832 \pm 10 \pm 58$
	120	no data available	

tion resolution $\sigma_{\mathrm{x}}'(3 \times 3)$ is obtained by unfolding the impact uncertainty from the fitted curve in figure 4.15. Likewise, an *uncorrected position resolution* $\sigma_{\mathrm{x}}(3 \times 3)$ is obtained using a fit on the uncorrected distribution. In this case the position offset correction improves the calorimeter position resolution over a whole cell in X from 360 ± 4 μm to 224 ± 3 μm.

Table 4.3 lists the corrected and uncorrected position resolutions over a whole cell (using 3×3 cell cluster in the first sampling) for both regions of the calorimeter. Table 4.4 lists the corresponding results for the second sampling. The results in tables 4.3 and 4.4 show that correcting the calorimeter reconstructed position with the offsets significantly improves the position resolution. These are the first results of position resolution over a whole cell for an RD3 accordion geometry calorimeter. The previous position resolution results [29] were obtained without considering the position offsets, and they are limited to a restricted portion of a cell.

The position resolution dependence on the impact within a cell was investigated, but no conclusions were reached due to a lack of experimental data. This study requires high statistics and an even coverage of several cells, which was not available.

The behaviour of the position resolution with respect to the electron energy is now treated. Beam energies of 20, 60, 90, 120 and 150 GeV are available. The electron data taken at 20, 60 and 90 GeV (one run each) does not cover a whole cell width in X. To minimize any systematic effect related to the position resolution dependence on impact in a cell, a fixed range within each cell is considered. To choose this range the calorimeter reconstructed position of electrons using a 3×3 cell cluster and all samplings $\mathrm{X}(3 \times 3)$ is studied in each of the 20, 60 and 90 GeV runs. From these position distributions a common impact range is selected that maximizes the electron statistics for each run. Subsequently all electron events in this study are restricted to the same range within each cell.

The same procedure, as described above for the position resolution across a whole cell is applied in this study. An electron sample is obtained as in section 4.2 and impact and position offset corrections are applied for each cell. The resulting calorimeter position resolutions are then parameterised using a function of energy and fitted using

$$\sigma_{\mathrm{x}} = a \oplus \frac{b}{\sqrt{E}}, \tag{4.10}$$

where E is in GeV and a and b are constants.

Results are listed in table 4.5. Figure 4.16 summarises the results obtained for experimental electron data, Monte Carlo simulations and the previous RD3 result.

Table 4.5: Fit parameters of the uncorrected and corrected calorimeter position resolution in X as a function of the electron energy for experimental data, Monte Carlo and previous RD3 results.

	$\sigma_x = a \oplus b/\sqrt{\mathrm{E}}$	
	a (μm)	b ($\mathrm{GeV}^{1/2} \cdot \mu$m)
$\sigma_{\mathrm{X}_1(3\times3)}$	0.5 ± 176	3754 ± 221
$\sigma_{\mathrm{X}'_1(3\times3)}$	137 ± 81	2981 ± 327
$\sigma_{\mathrm{X}_2(3\times3)}$	220 ± 77	5234 ± 301
$\sigma_{\mathrm{X}'_2(3\times3)}$	0 ± 164	5044 ± 223
Previous RD3 result ($\sigma_{\mathrm{X}_1(5\times5)}$)	70 ± 4	4380 ± 360

From figure 4.16 the following observations can be made:

- The uncorrected position reconstruction performance agrees with the published RD3 result [29];
- The position offset correction significantly improves the position reconstruction performance of the calorimeter prototype;
- The experimental corrected position resolution agrees well with the Monte Carlo prediction;
- The 120 GeV data point exhibits a systematic tendency towards a better position resolution than the other data or simulation points would suggest.

The previous RD3 result was obtained using a 5×5 cell cluster in the first sampling. A 5×5 cell cluster is less sensitive to lateral shower fluctuations and should be more accurate than a 3×3 cell cluster. The uncorrected calorimeter position resolution using a 3×3 cell cluster is similar to this RD3 result which suggests that for position measurements this cluster size is adequate. A test of a 5×5 cell cluster is not possible in this study due to experimental restrictions. The position offset correction is seen to be a useful correction to enhance the position reconstruction performance of the calorimeter. The agreement between Monte Carlo predictions and the experimental results also encourages the use of Monte Carlo simulations to study other accordion geometries. The systematic tendency of the 120 GeV data position resolution to lie below the curve is not understood. The selection of electrons is identical as in other runs and the same beam line is used. The 120 GeV runs were taken in the second beam period, and adjustment or resetting of the encoders led to differing impact statistics within each cell when comparing to the 150 GeV runs. Therefore, it is possible that the 120 GeV electrons impact a low position resolution area of each cell which would account for the difference in performance for these runs.

The results above use position offset corrections on the data that generated the particular offsets. This can potentially lead to an overestimate of the position reconstruction performance of the calorimeter. The following test is performed to test whether the position offsets can be used globally.

Particular cells (*calibration cells*) that have maximal electron coverage and are the centre of a problem free 3×3 cell cluster are selected in each calorimeter region. Position offsets of electrons for each calibration cell are calculated in both the first and second samplings using the method above to form a *calibration set.* The position offset corrected position resolutions in the first and second samplings of runs different from the ones used to form calibration sets are calculated. The results, shown in table 4.6 are expressed as the percentage improvement of the position resolution after the position offset correction is made. These results show that the position offset correction applied to independent cells result in a smaller improvement in the case of 150 GeV electrons. In the second sampling of the two sampling region, we note that

Table 4.6: Position offset corrected position resolutions in the first and second samplings of runs different from the ones used to form the calibration sets, expressed in percent improvement. The errors are systematic.

Region	Energy (GeV)	Percent improvement $\sigma_{\mathrm{X}'_1(3\times3)}(\%)$	Percent improvement $\sigma_{\mathrm{X}'_2}(3\times3)(\%)$
Two sampling	150 GeV	1 ± 3	-3 ± 8
Three sampling	150 GeV	2 ± 7	4 ± 5
	120 GeV	18 ± 17	13 ± 10

EM showers have widened at this depth and the position resolution is dominated by fluctuations. The 120 GeV results in the three sampling region show good position resolution improvement (a cell corrected with its own data typically shows an improvement of $\sim 13 \pm 6\%$) but the results are dominated by large systematic errors which are thought to arise because of differences in beam coverage between cells. Although an attempt is made to maximize the electron coverage of the calibration cell the subsequent runs have slightly differing impact statistics. Events that fall outside the calibration set coverage remain uncorrected.

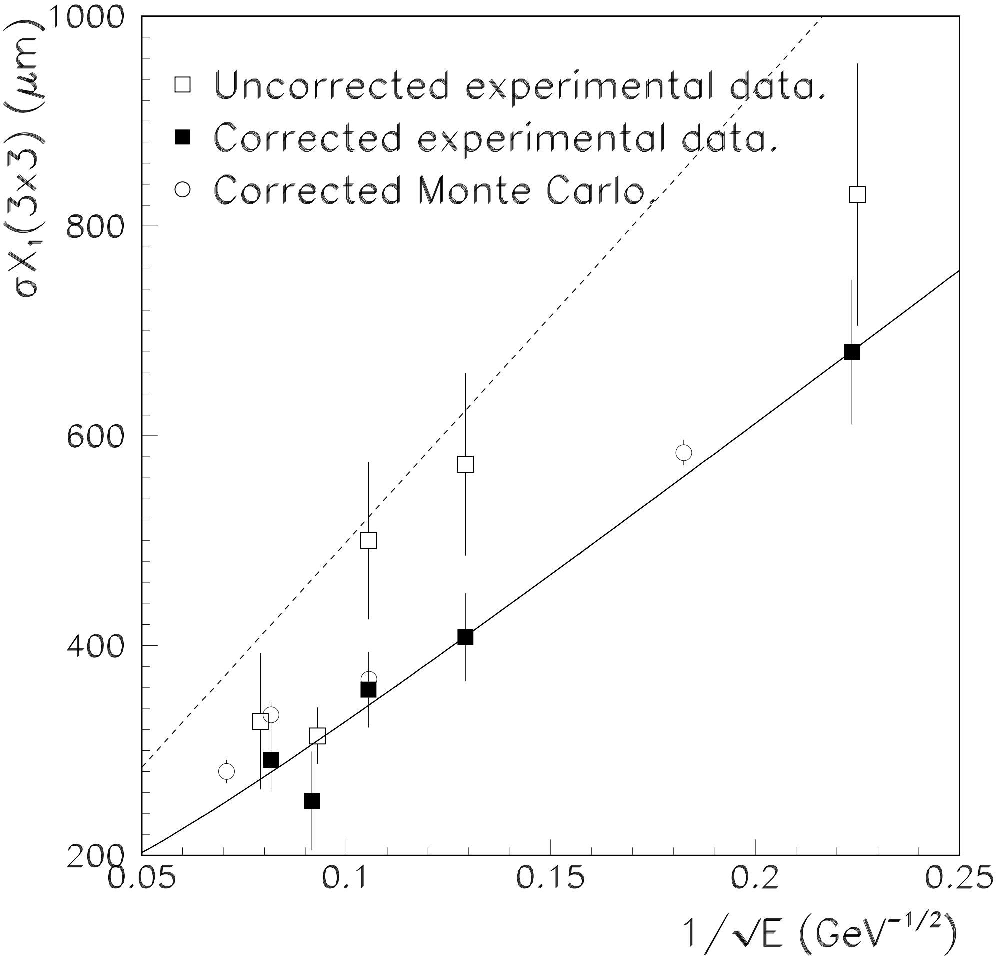

Figure 4.16: Position resolution of the calorimeter in the X direction for different electron energies. The solid (open) squares are the corrected (uncorrected) experimental resolutions using $X_1(3 \times 3)$ with combined statistical and systematic errors shown. The solid line is a fit to the corrected experimental resolutions using equation 4.10. The open circles are the corrected Monte Carlo resolutions using $X_1(3\times3)$. The dashed line corresponds to the published RD3 results [29]

4.4 Angular Reconstruction

As well as providing energy and position measurements the accordion geometry calorimeter can be used to determine the angle of incidence of a particle. An EM shower develops in the calorimeter along the incoming particle direction. Therefore the relative shower position in successive samplings will have a lateral displacement (d) proportional to the incidence angle. This lateral displacement (neglecting position offsets) is directly proportional to the incidence angle θ :

$$\frac{d}{L} = \tan\theta \simeq \theta . \tag{4.11}$$

The constant L in equation 4.11, referred to as the *lever arm*, is the longitudinal distance between the shower centroids in each sampling. It therefore depends on the longitudinal profile of the shower produced by the incoming particle with incidence angle θ.

To study the angular reconstruction performance of the calorimeter prototype the lever arm has to be found. Data runs (called angular runs) with electrons incident on the calorimeter at different angles were taken for three different impact regions on the calorimeter; one in the three sampling region and two in the two sampling region. For each impact region, data were taken for three incidence angles each separated by 2° for electrons of 20, 60 and 120 GeV. Such angular runs were only carried out for angles in the X direction; the angular resolution in the Y direction cannot therefore be studied. Data taken in the two sampling region are not adequate for a study of the angular reconstruction. Therefore the two sampling region is not considered.

Electrons are selected from each angular run following the method outlined in section 4.2 and the distribution of $d = \mathrm{X}_2(3\times3)–\mathrm{X}_1(3\times3)$ is studied, where $\mathrm{X}_2(3\times3)$ and $\mathrm{X}_1(3 \times 3)$ are the calorimeter reconstructed shower position using a 3×3 cell

Table 4.7: Resulting lever arm obtained from angular runs in the three sampling region for 3 different electron energies.

Energy	$d = a + L\,\theta$	
(GeV)	a (mm)	L (mm/mrad)
120	1.01 ± 0.01	97.3 ± 0.3
60	1.17 ± 0.01	98.4 ± 0.5
20	0.67 ± 0.02	103.6 ± 0.7

cluster in the second and first sampling respectively. To reduce the clustering effect the most energetic cell in the first and second sampling are required to be the same. The events cut by this requirement were not used in the calculation of the lever arm. The measurement of d for different angles of incidence θ are fitted to a relation of the form

$$d \;=\; a + L\theta\,, \tag{4.12}$$

where a is a constant associated with the neglected position offsets. The lever arm L and constant a are obtained for the three sampling region and the results are shown in table 4.7.

With increasing particle energy E, the depth corresponding to maximum deposited energy grows as $\ln E$. Assuming that this maximum occurs in the first sampling (which is shown to be the case from Monte Carlo simulations for all the energies studied), the centroid in depth in the first sampling also approximately follows $\ln E$. In the second sampling, the depth centroid will be close to its face. From these observations the lever arm is expected to decrease in length.

The values shown in table 4.7 are fitted to

$$L \;=\; a + b * \ln E \tag{4.13}$$

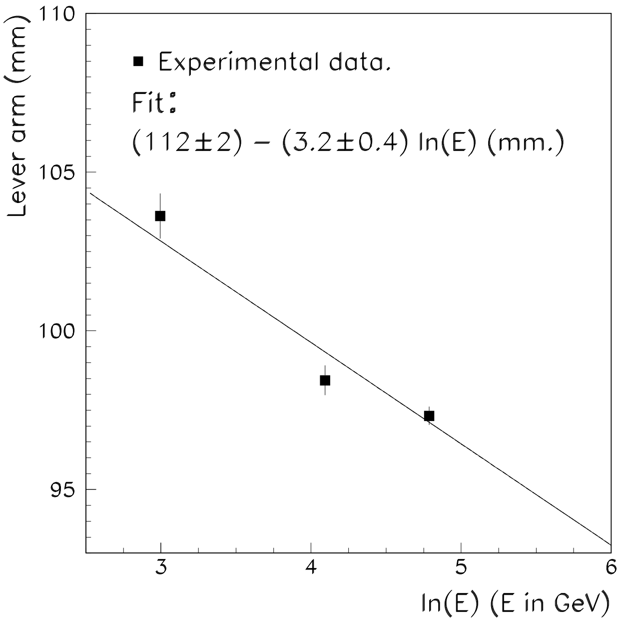

Figure 4.17: Experimental lever arms for the three sampling region. Statistical errors shown.

in an attempt to parameterize the energy dependence of the lever arm. Results are shown in figure 4.17.

With a knowledge of the lever arm for the experimental energy range the angular reconstruction performance can now be studied. The incidence angle θ, obtained from equation 4.13, is then studied for data runs different from the angular runs. The width of the reconstructed θ for these runs is the angular resolution and contains a small contribution from the error on the lever arm (see table 4.8).

So far the position offsets have been ignored in this study. The basic problem in trying to introduce the offset correction to this study lies with the impact

Table 4.8: Experimental calorimeter angular resolutions for the three sampling region. The first error is statistical and the second is systematic.

Energy (GeV)	σ_θ (mrad)
150	$5.99 \pm 0.10 \pm 0.21$
120	$6.19 \pm 0.13 \pm 0.42$
90	$6.93 \pm 0.09 \pm 0.35$
60	$8.35 \pm 0.10 \pm 0.42$
20	$17.14 \pm 0.34 \pm 0.86$

measurement. There is no information, except by comparison of position offsets for data and simulations, on the angle of the calorimeter with respect to the beam. The impact in the second sampling cannot be predicted from beam chamber and encoder information since the angle of the calorimeter with respect to the beam is needed.

To introduce position offset corrections to this study several steps are taken. The position offsets of figure 4.14 for an angular run are checked. Using experimental position offset results and comparing with Monte Carlo offset predictions the actual angle of incidence is found, allowing calculation of the impact in the second sampling. The position offsets of both the first and second samplings are then known and the calorimeter reconstructed position can be corrected.

Figure 4.18 shows the improvement on $X_2(3 \times 3) - X_1(3 \times 3)$ when position offset corrections are applied. Note in figure 4.18 that the asymmetric tail to the left of the distribution is reduced by the position offset corrections. Runs other than those used to calibrate the position offsets are selected. The particle angle of incidence is calculated using the experimentally determined lever arm and the position offset corrections for both samplings . The results are shown in table 4.9. The results from tables 4.8 and 4.9 are plotted along with the previous RD3 result

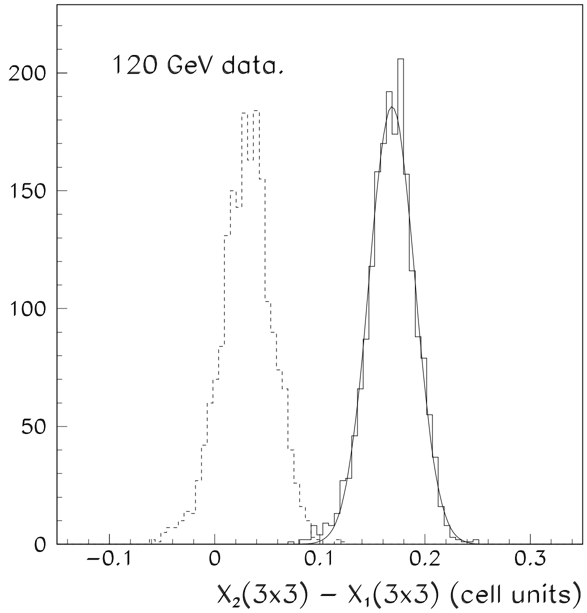

Figure 4.18: The solid (dashed) line shows $X_2(3 \times 3) - X_1(3 \times 3)$ after (before) position offset corrections are applied.

Table 4.9: Angular resolution after position offset corrections. The first error is statistical and the second is systematic.

Energy (GeV)	σ_θ (mrad)
150	$5.6 \pm 0.1 \pm 2.5$
120	$6.0 \pm 0.1 \pm 0.7$
90	$6.1 \pm 0.1 \pm 2.5$
60	$7.6 \pm 0.1 \pm 1.8$
20	$14.1 \pm 2.3 \pm 2.2$

in figure 4.19. The fit to uncorrected experimental data used in figure 4.19 is

$$\sigma_\theta = \frac{67.4 \pm 2.5}{\sqrt{E}} \oplus \frac{139 \pm 57}{E} \tag{4.14}$$

with E in GeV and σ_θ in mrad. The first term is the sampling term and depends on shower fluctuations; the second term is probably caused by the electronic noise of the readout chain.

The fit result shown in figure 4.19 cannot be directly compared to the published RD3 [30] since the number of samplings is different. The angular resolution in the three sampling region is superior to that in the two sampling region because of a better energy sharing between the front and second samplings for the electron energies studied.

The position offset corrections are seen to improve the angular resolutions. Only one energy could be studied in this case because the data taken allows calibration of a cell for both lever arm and position offsets at a single energy. The systematic errors introduced when studying the angular resolution at other energies and in different cells are large (see table 4.9), pointing to the need for good calibration data.

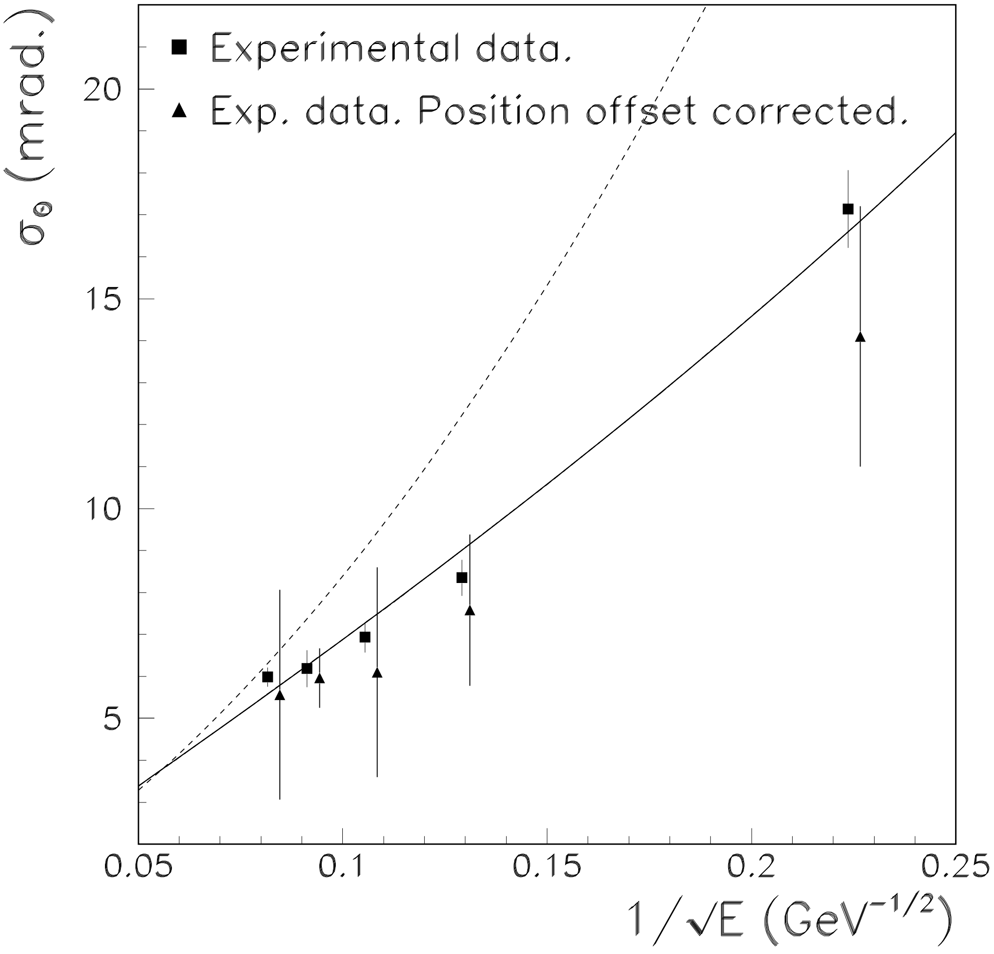

Figure 4.19: Calorimeter angular resolution as a function of energy for experimental data in the three sampling region (squares and solid fitted curve). The position offset corrected angular resolutions are also shown (triangles). The dashed curve is the previous RD3 result in the two sampling region [30].

Chapter 5

Conclusions

An electromagnetic calorimeter prototype using a novel accordion geometry was exposed to energetic electron beams and its spatial reconstruction performance was studied. Geometrical effects (*position offsets*) due to the accordion folds were observed in both experimental data and Monte Carlo simulations and for the first time corrected for to improve the calorimeter spatial reconstruction.

A position resolution in the direction of the accordion folds in the first sampling of $(3.8 \pm 0.2)/\sqrt{E}$ mm was found, which agrees well with the previous published result of $(4.4 \pm 0.4)/\sqrt{E}$ mm [29] (E in GeV). The new result was obtained using a smaller cluster of cells. This smaller cluster can be appropriate for a fast ATLAS event trigger. The position resolution after position offset correction was found to improve to $(3.0 \pm 0.3)/\sqrt{E}$ mm, stressing the importance of a good knowledge of the geometrical offsets.

The calorimeter position reconstruction performance was also studied with data covering a whole cell. At electron energies of 120 and 150 GeV the position resolution in the direction of the accordion folds, using the first (second) calorimeter sampling, is measured to be ~ 0.5 (~ 0.8) mm after position offset correction. In the direction parallel to the accordion folds the position resolution in the first calorimeter sampling was found to be a factor of ~ 1.2 worse. These results demonstrate the superior position reconstruction performance due to the accordion folds.

The intrinsic accuracy of the prototype to reconstruct the angle of an incident electron was found to be

$$\sigma_\theta\,(\mathrm{mrad}) = \frac{67.4 \pm 2.5}{\sqrt{E}} \oplus \frac{139 \pm 57}{E},$$

where E is in GeV, meeting the $100/\sqrt{E}$ mrad requirement set by ATLAS [26]. This dependence could not be directly compared to the previous result since the configuration of the detector is different in each case.

In both the position and angular resolution studies a global position offset correction was made. This resulted in improved performance in both cases but the result was dominated by large systematic uncertainties. These uncertainties were caused by imperfect position offset calibration data and differences in cell to cell energy calibration. Complete electron coverage of cells and better knowledge of the electron impact prediction would allow the formation of a global calibration set and reduce the systematic uncertainty. The energy parameterisation of these corrected resolutions are not quoted for these reasons.

The results obtained in this study show that the accordion geometry calorimeter has exceptional position and angular reconstruction capabilities that meet the criteria for an ATLAS EM barrel calorimeter. The experimental observation and correction of the position offsets due to the accordion geometry will have to be considered in future tests of other accordion prototypes. The agreement of experimental data and Monte Carlo simulations encourages the use of these simulations to further develop and optimise the accordion calorimeter which will be an important part of the ATLAS detector at LHC.

Bibliography

[1] S. L. Glashow, Partial-Symmetries of Weak Interactions. *Nucl. Phys.*, **22** (1961), p.579;
A. Salam in Elementary Particle Theory.
ed. N. Svartholm. (Almquist and Wiksell, Stockholm, 1968);
S. Weinberg, A Model of Leptons *Phys. Rev. Lett.*, **19** (1967), p.1264.

[2] G. Arnison *et al.*, Experimental Observation of Isolated Large Transverse Energy Electrons with Associated Missing Energy at $\sqrt{s} = 540$ GeV. *Phys. Lett.*, 122B (1983), p.103.

[3] G. Arnison *et al.*, Experimental Observation of Lepton Pairs of Invariant Mass Around 95GeV/c^2 at the CERN SPS Collider. *Phys. Lett.*, 126B (1983), p.398.

[4] P. W. Higgs, Broken Symmetries, Massless Particles and Gauge Fields. *Phys. Lett.* , **12** (1964), p.132.
Broken Symmetries and the Masses of the Gauge Bosons. *Phys. Rev. Lett.*, **13** (1964), p.508.
Spontaneous Symmetry Breakdown without Massless Bosons. *Phys. Rev.*, **145** (1966), p.1156.

[5] Particle Data Group, Review of Particle Properties. *Physical Review D: Particles and Fields*, **45D** (1992).

[6] For reviews, see:
M. Sher, Electroweak Higgs Potentials and Vacuum Stability. *Phys. Rep.*, **179** (1989), p.273. and
J. Gunion *et al.* , *The Higgs Hunter's Guide.*, (Addison-Wesley, Redwood City, 1990).

[7] A. Carter, talk given at the IoP Conference on Nuclear and Particle Physics, Glasgow, 1993.

[8] The LEP Electroweak Working Group,
Updated Parameters of the Z^0 Resonance from Combined Preliminary Data of the LEP Experiments. CERN/PPE/93-157, 26 August, 1993

[9] F. Abe *et al.*, Top Quark Search in the electron + Jets channel in proton-antiproton collisions at $\sqrt{s} = 1.8$ TeV. *Phys. Rev.*, **D43**, (1991), p.664.

[10] M. Kobayashi and T. Maskawa, CP-Voilation in the Renormalizable Theory of Weak Interaction. *Prog. Theor. Phys.* , **49**, (1973), p.652.
N. Cabibbo, Unitary Symmetry and Leptonic Decays. *Phys. Rev. Lett.*, **10**, (1963), p.531.

[11] See for example the following review:
J. R. Carter, *Precision tests of the Standard Model at LEP*, Proceedings of The Joint International Lepton-Photon Symposium and Europhysics Conference on High Energy Physics, Geneva, Switzerland, 25 July - 1 August 1991, World Scientific.

[12] The LHC Study Group, *Design Study of the Large Hadron Collider (LHC)*, CERN/91-03, 2 May 1991.

[13] The ATLAS Collaboration, *Letter of Intent*, CERN/LHCC/92-4, LHCC/I 2, 1 October 1992.

[14] For a general overview of physics, detectors and detector subsystems at future hadron colliders see,
P. Jenni and J. White, Physics and Experimental Challenge of Future Hadron Colliders. *Proceedings of the 1993 Lake Louise Winter Institute.*, held in Lake Louise, Alberta, 21st to 27th of February, 1993.

[15] A. Dobado, The Mass and Width of the Higgs in the Strongly Interacting Minimal Standard Model. *Phys. Lett.* , **237** (1990), p.457-462.

[16] D. P. Roy, Discovery Limit of the Charged Higgs Boson via Top Quark Decay at Future Hadron Colliders. *Phys. Lett.*, **B283**, (1992), p.403-410.

[17] A. Bartl *et al.*, Signatures of Gluinos and Squarks at Proton-Proton Colliders. *Z. Phys.*, **C52**, (1991), p.477-485.

[18] H. A. Bethe and W. Heitler, *Proc. Roy. Soc.* A146 (1934), p.83.

[19] Y. S. Tsai, Pair Production and Bremsstrahlung of Charged Leptons. *Rev. Mod. Phys.*, **46** (1974), p.815.

[20] W. R. Nelson *et al.*, Electron-Induced Cascade Showers in Copper and Lead at 1 GeV. *Phys. Rev.*, **149** (1966), p.201.

[21] D. Perkins, *Introduction to high energy physics*, (3rd ed.) (Addison-Wesley Publishing Company. Menlo Park, 1987).

[22] B. Rossi, *High Energy Particles*, (Prentice Hall, New York, 1964).

[23] U. Amaldi, Fluctuations in Calorimetry Measurements. *Physica Scripta,* **23** (1981), p.409-424.

[24] G. Nilsson *et al.*, A Phenomenological Investigation of the Shower Particle Particle Pseudorapidity Fluctuations in Hadron-Nucleus Collisions. *Nuc. Phys.*, **B195** (1982), p.203.

[25] R. Wigmans, *Advances in Hadron Calorimetry*, 1991, CERN-PPE-91-39.

[26] L. Fayard, and G. Unal, Search for Higgs Decay into Photons with EAGLE. EAGLE note, PHYS-NO-001.

[27] W. J. Willis and V. Radeka, Liquid Argon Ionization Chambers as Total Absorption Detectors. *Nucl. Inst. and Meth.*, **120** (1974), p. 221-236.

[28] T. Doke *et al.*, Average Energy Expended per Ion Pair in Liquid Argon, *Phys. Rev.*, **A9** (1974), p.1438.

[29] B. Aubert *et al.*, Performance of a liquid argon electromagnetic calorimeter with an "accordion" geometry. *Nucl. Inst. and Meth.*, **A309** (1991), p.438-449.

[30] B. Aubert *et al.*, Performance of a liquid argon accordion calorimeter with fast readout. *Nucl. Inst. and Meth.*, **A321** (1992), p. 467-478.

[31] B. Aubert *et al.*, Performance of a Liquid Argon Calorimeter with a Cylindrical Accordion Geometry. *Nucl. Inst. and Meth.*, **A325** (1993), p.116-128.

[32] B. Aubert *et al.*, Performance of a Liquid Argon Preshower Detector Integrated with an Accordion Calorimeter. *Nucl. Inst. and Meth.*, **A330** (1993), p.405-415.

[33] B. Yu and V. Radeka (editors), SSC R&D at BNL, BNL52244 (1990).

[34] D. V. Camin *et al.*, Gallium Arsenide charge sensitive preamplifier for operation in a wide low temperature range. *Nucl. Inst. and Meth.*, **A289** (1990), p.426-437.

[35] S. Rescia, and V. Radeka, (1988). Speed and noise limits in ionization chamber calorimeters. *Nucl. Inst. and Meth.*, **A265** (1988), p.228-242.

[36] S. Howe, L. S. Miller and W. E. Spear, Charge transport in Solid and Liquid Ar, Kr, and Xe. *Phys. Rev.*, **166** (1968), p.871-878.

[37] H. J. Specht, The Helios experiment. *Nucl. phys.* **A447** (1986), p.387-391.

[38] A. Manarin, and G. Vismara, The delay wire chamber description. LEP/BI-TA/Note 85-3.

[39] Application Software Group, Computing and Networks division, CERN. (July, 1992) PAW, CERN program library long writeup Q121.

[40] Application Software Group, Computing and Networks division, CERN. (January, 1992) GEANT User's Guide, CERN program library long writeup Q123.

[41] M. Lefebvre, G. Parrour and P. Pétroff, Electromagnetic Liquid Argon Accordion Calorimeter Simulation. *RD3 note 41*, (1993).

Appendix A

Calculation of error on beam chamber hit.

Each one of the three beam chambers [38] in front of the calorimeter return the x and y coordinate of a charged particle passing through them. The locations of these beam chambers along the beam line in Z are precisely known from survey information. Using the x,y position of a particle in each chamber its trajectory is deduced and extrapolated to give the particle impact at the calorimeter face. The uncertainty on this impact point calculation is considered here.

We assume the abscissa to run along the Z (beam line) axis and the ordinate to run in either the X or Y direction. A set of data z_i, y_i $(i = 1$ to $3)$ is fitted with

$$y_i = \beta_1 + \beta_2 z_i \,, \tag{A.1}$$

where z_i is the Z value for chamber 'i', and y_i is the particle position in X or Y given by chamber 'i'.

Using the least squares fit method the best estimators of the parameters β_1 and β_2 are given by

$$\hat{\beta}_1 = \langle y \rangle - \hat{\beta}_2 \langle z \rangle$$

and

$$\hat{\beta}_2 = \frac{\langle zy \rangle - \langle z \rangle \langle y \rangle}{\langle z^2 \rangle - \langle z \rangle^2}$$

We now have a general relation between y and z,

$$y = \hat{\beta}_1 + \hat{\beta}_2 z \, . \tag{A.2}$$

We wish to find y at the calorimeter face, which is located at $z = z_0$. The uncertainty on the impact position is the variance in y. From equation A.2, error propagation theory gives

$$\mathrm{Var}(y) = \mathrm{Var}(\hat{\beta}_1) + \mathrm{Var}(\hat{\beta}_1) z_0^2 + 2 z_0 \mathrm{cov}(\hat{\beta}_1, \hat{\beta}_2) \, . \tag{A.3}$$

The variances of $\hat{\beta}_1$ and $\hat{\beta}_2$ are calculated to be

$$\mathrm{Var}(\hat{\beta}_1) = \frac{1}{n} \frac{\sigma^2 \langle z^2 \rangle}{\langle (z - \langle z \rangle)^2 \rangle} \, . \tag{A.4}$$

$$\mathrm{Var}(\hat{\beta}_2) = \frac{1}{n} \frac{\sigma^2}{\langle (z - \langle z \rangle)^2 \rangle} \, , \tag{A.5}$$

and the covariance is given by

$$\mathrm{cov}(\hat{\beta}_1, \hat{\beta}_2) = -\frac{1}{n} \frac{\sigma^2 \langle z^2 \rangle}{\langle (z - \langle z \rangle)^2 \rangle} \, , \tag{A.6}$$

where σ is the uncertainty on a single beam chamber measurement of X or Y.

Substituting equations A.4 to A.6 into equation A.3 we obtain

$$\mathrm{Var}(y) = \frac{1}{n} \frac{\sigma^2 \langle (z - z_0^2)) \rangle}{\langle (z - \langle z \rangle)^2 \rangle} \, , \tag{A.7}$$

which allows us to calculate the uncertainty on the beam chamber impact. For the test beam setup used at CERN all the quantities in equation A.7 are available, which yields an uncertainty is 255 μm in X and 260 μm in Y for the beam chamber impact.

Appendix B

Calculation of pion background and error

The presence of pion events in the electron sample can worsen the position resolution due to the larger fluctuations of hadronic showers. The pion contamination of electron samples is estimated below.

Let N be the number of events in an electron sample. The charged pion rejection factors R_1, R_2 and R_{12} are determined from application of the longitudinal and lateral cuts separately and concurrently on a sample of pions whose deposited energy is close to the electron energy peak (see figure 4.5). We have

$$N = S + B\,, \tag{B.1}$$

where S and B are the signal (electrons) and background (charged pions) contents of the electron sample.

After applying the longitudinal cut to the electron sample we have

$$N_1 = \varepsilon_1 S + \frac{B}{R_1}\,, \tag{B.2}$$

where N_1 is the number of events left after the cut, ε_1 and R_1 are respectively the electron efficiency and the charged pion rejection of the cut.

Similarly, applying the lateral cut we have

$$N_2 = \varepsilon_2 S + \frac{B}{R_2}\,. \tag{B.3}$$

Equations B.1, B.2 and B.3 contain four unknowns: S, B, ε_1, and ε_2. Another equation is needed to solve the system. Applying the cuts simultaneously, we get

$$N_{12} = \varepsilon_{12} S + \frac{B}{R_{12}}\,. \tag{B.4}$$

Neglecting the small correlations found between both cuts (see below and table B.1) we can use

$$\varepsilon_{12} = \varepsilon_1 \varepsilon_2\,,$$

$$R_{12} = R_1 R_2\,.$$

Equations B.1 to B.4 can be rearranged as a function of B, the pion background, giving

$$(R_{12} - R_1R_2)B^2 + (R_1N_2 - R_{12}N - N_{12} - R_2N_1)B + (N_{12}N - N_1N_2) = 0\,, \tag{B.5}$$

which is easily solved for B. S and ε_n $(n = 1, 2, 12)$ are then found using equation B.1 and equations B.2 to B.4:

$$S = N - B \quad ; \quad \varepsilon_n = \frac{N_n - R_nB}{S}\,.$$

The pion contamination $\frac{B}{N}$ is readily obtained.

We now need to consider the error on B. The following substitutions are made in equation B.5:

$$a = R_{12} - R_1R_2\,; \tag{B.6}$$

$$b = R_1N_2 - R_{12}N - N_{12} - R_2N_1\,; \tag{B.7}$$

$$c = N_{12}N - N_1N_2\,. \tag{B.8}$$

The error on B can be calculated using the derivative of equation B.5 which yields

$$dB = \frac{-\{B^2 da + B db + dc\}}{2Ba + b} \,. \tag{B.9}$$

Using error propagation theory the errors on a, b and c (da, db and dc respectively) are calculated giving

$$da^2 = (dR_{12})^2 + (R_1 dR_2)^2 + (R_2 dR_1)^2 \,, \tag{B.10}$$

$$db^2 = (N_2 dR_1)^2 + (N_1 dR_2)^2 + (N dR_{12})^2 \,, \tag{B.11}$$

$$dc^2 = 0 \,. \tag{B.12}$$

Equation B.12 results from the definition of c in terms of exactly known quantities. The results from B.10, B.11 and B.12 are substituted into B.9 and the uncertainty dB can be calculated. The error on the pion contamination $\frac{dB}{N}$ is therefore obtained. Results are shown in table B.1 for various data samples.

The correlation of the lateral and longitudinal cuts is considered next. The correlation coefficient for two variables α_a , α_b is defined as

$$\frac{\langle(\alpha_a - \langle\alpha_a\rangle)(\alpha_b - \langle\alpha_b\rangle)\rangle}{\sqrt{\langle(\alpha_a - \langle\alpha_a\rangle)^2\rangle\langle(\alpha_b - \langle\alpha_b\rangle)^2\rangle}} \,. \tag{B.13}$$

In this case α_a and α_b refer to the longitudinal and lateral cuts for charged pions in a sample close to the electron peak. These values are calculated in a binary form that is with $\alpha_i = 1$ corresponding to events that pass the cut (mainly electrons) and $\alpha_i = 0$ for events that are cut (mainly pions). The cut correlation for various representative data samples are shown in table B.1.

The pion contamination of the electron samples used in this analysis is found to be small and is neglected.

Table B.1: The pion contamination of selected data samples.

Energy (GeV)	Pion contamination (%)	Cut Correlation (%)
150	0.2 ± 0.2	2
150	$< 0.1 \pm 0.1$	4
120	$< 0.1 \pm 0.1$	5
90	3 ± 1	4
60	$< 0.1 \pm 0.1$	< 1
20	$< 0.1 \pm 0.1$	< 1